Biophotonic implants for NIR-imaging

Master's thesis

Natalia Antonova

Intelligent Materials Chemistry

Department of Chemistry

University of Turku

June 2025

The originality of this thesis has been checked in accordance with the University of Turku quality assurance system using the Turnitin Originality Check service.

Master's thesis

Subject: Chemistry

Author: Natalia Antonova

Title: Biophotonic Implants for NIR-imaging

Supervisors: Mika Lastusaari, Sami Vuori and Hannah Byron

Number of pages: 42 p.

Date: June 2025

Bioactive glasses (BAGs) are implantable biomaterials that promote bone tissue regeneration and healing. Various radiographic imaging techniques are commonly used to monitor the state of BAGs after implantation. However, due to the weak contrast between the biomaterial and bone tissue, the information obtained from radiographic images is limited. The fabrication of biophotonic BAGs by doping phosphor materials into a glass matrix allows the use of optical imaging techniques or combinations of imaging techniques for the non-invasive real-time monitoring of implants. During optical imaging, light encounters various photophysical processes, such as reflection, scattering, and absorption, when it passes through biological tissues, which significantly reduce its intensity. However, NIR light is the least susceptible to these processes. Therefore, today, the primary challenge for researchers is the development and fabrication of phosphors with the desired optical properties in the NIR region.

During this work, MgO and $Mg_{14}Ge_5O_{24}$ NIR phosphors doped with both rare earth and transition metal ions were synthesized. Samples with the best NIR optical properties were selected and doped into a NaPSrO glass matrix. The fabricated glass-phosphor composites demonstrated promising results, indicating that they can be used as biophotonic implants for NIR optical imaging.

Keywords: bioactive glass, biophotonic implants, NIR optical imaging, NIR-phosphors, doped MgO, doped $Mg_{14}Ge_5O_{24}$, 3D scaffolds, glass-phosphor composites

Table of Contents

Abbreviations

HA = Hydroxyapatite

BAG = Bioactive glass

NIR = Near-infrared

UV = Ultraviolet

LD = Laser diode

LED = Light-emitting diode

CCD = charge-coupled device

IR = Infrared

PeL = Persistent luminescence

XRD = X-ray diffraction

XRF = X-ray fluorescence

PL = Photoluminescence

TL = Thermoluminescence

OSL = Optically stimulated luminescence

XEOL = X-ray excited optical luminescence

CL = Cathodoluminescence

SCS = Solution combustion synthesis

MGO = $Mg_{14}Ge_5O_{24}$

1. Introduction

1.1 Implants and three generations of biomaterials

Implants are artificially created, non-biological materials inserted into the host body to replace lost or damaged vital body parts and restore their normal functions.[1] According to archaeological findings, in the era of ancient civilizations, people used readily available natural materials as the first primitive implants, the main task of which was to restore the basic functions of the body. Examples of such materials were stones, shells, animal bones, wood, and various types of metals.[2] With the development of medicine and science, it has become clear that the implant material plays a significant role in the success of implant integration, longevity, and survival because it directly interacts with the biological tissues.[3] Therefore, the primary materials of modern implants are biomaterials, the main requirement for which is biocompatibility, that is, the ability of the material to perform its function without causing significant harm to the host's body.[1] In addition, such materials must be non-toxic, non-carcinogenic, easy to fabricate and use.[3]

From the 20th century to the present day, three generations of biomaterials have been developed, each with clinical requirements and purposes.[4] The main purpose of first-generation biomaterials is to perform the functions of the replaced tissue, minimally interacting with biological fluids and not causing any harm to the host's body.[3] Therefore, these biomaterials are biologically and chemically inert and they have similar physical properties to the replaced tissue.[4] Examples of inert biomaterials are stainless steel (SS), Co-alloys, Alumina (Al_2O_3),[3] Zirconia (ZrO_2), phosphorylcholine, and some types of polyethylene polymers.[1] In contrast, the second generation of biomaterials consists of bioactive components, which directly interact with the native tissue of the host, forming a strong bond with it.[4] Examples of such materials are hydroxyapatite (HA), tricalcium phosphate (TCP), bioactive glasses,[1] and Ti-alloys[3]. Additionally, this generation also includes biodegradable materials, such as polymers composed of polylactic acid (PLA) or polyglycolic acid (PGA), which are resorbed in the host body and replaced by biological tissue.[4] Biomaterials of the first two generations have significantly improved the quality of implants themselves and raised the level of implantology, but the problem of limited longevity has not been resolved. Therefore, the development of new third-generation biomaterials has become a main challenge for researchers in recent decades.[3,4]

The main difference of third-generation biomaterials is that they are temporary, implantable bioactive structures that interact with the biological system and biodegrade over time. This stimulates the cellular growth of the host's native tissue, thereby promoting its complete or partial regeneration.[4] Basically, these biomaterials are three-dimensional porous structures with mechanical properties

similar to the surrounding biological host tissue, as well as with controlled biodegradability.[5] Examples of such materials are Mg-alloys,[6] mesoporous and macroporous scaffolds based on bioactive glasses, nanobioactive glasses,[7,4] biopolymer and bioceramic composite materials.[5]

As this work is closely related to bioactive glasses, the following chapters will focus on this biomaterial, its properties, advantages, and disadvantages, as well as attempts to modify them.

1.2 Bioactive glasses

Bioactive glasses (BAG) belong to the second and third generations of biomaterials;[8] they are unique bioactive materials that differ from conventional types of glass by their poor chemical durability. Therefore, they have the ability to chemically interact with biological fluids, gradually dissolving and forming a strong bond with the surrounding host tissues, promoting their regeneration and healing.[9] Unlike other types of bioactive materials, they form a hydroxyapatite (HA) layer on the glass surface during the dissolution. This layer can form a strong bond with the bone tissues because it has a similar chemical composition and structure to the mineral phase of bone (bioapatite).[8,9] In addition, due to the amorphous structure of bioactive glass, it is possible to control the rate and mechanism of its dissolution by changing the composition of the glass material or the ratio of its starting reagents.[10,11] Also, by doping bioactive glasses with various ions, their properties can be purposefully modified.[12] For instance, doping with Ag^{+}, Ce^{3+}, and Zn^{2+} ions gives the glass antibacterial properties.[9]

There are three main types of bioactive glass, which differ in their chemical composition and properties. They are silicate, borate, and phosphate bioactive glasses.[11] The first and most studied material is the silicate-based glass 45S5 with a composition of $Na_2O–CaO–P_2O_5–SiO_2$, developed by Hench in 1969.[8,13] Compared to other types of BAGs, it has richer chemical durability because during its dissolution a Si-rich layer is first formed and then the HA layer begins to form on top of it.[8] Thus, due to its relatively high strength and long-term stability, this type of glass is used as orthopedic and dental implants, as well as a coating material for metal implants.[13,14,15] In contrast, borate-based glasses with a chemical composition of $B_2O_3–CaO–Na_2O–P_2O_5$ have poor chemical durability since they degrade faster *in vivo*, forming the HA layer.[10,16] Therefore, they are used as temporary 3D scaffolds to stimulate regeneration or healing of biological tissues, as well as in drug delivery systems because they more easily release therapeutic ions.[16–18] Another advantage of this type of glass is that the rate of its dissolution *in vivo* can be controlled by changing the composition of the glass, thereby ensuring the stability of the implant for the required time.[10] In turn, phosphate-based glasses with a composition of $CaO–Na_2O–P_2O_5$ are classified as third-generation biomaterials because they have the ability to completely resorb in the host body. The main advantages of these glasses are that they have

the poorest chemical durability among other types of BAGs, and their chemical composition is close to the mineral phase of bone tissue.[19] However, the phosphate glasses are less stable than the borate BAGs, even though their dissolution rate can also be controlled.[10,11] Phosphate glasses are typically used as 3D scaffolds in tissue engineering and drug delivery system.[19,20,21]

Nowadays, bioactive glasses are widely used in various fields of medicine and clinical research, demonstrating promising results.[15] Radiographic methods are most commonly used to monitor the integration of bioactive glasses, their gradual degradation, the formation of the HA layer, and the growth of new bone after surgery.[22] In radiography, the contrast between the implant and biological tissue plays a significant role; therefore, in this context, the main advantage of BAG may become a disadvantage.[22,23] The formed HA layer on the BAG surface is similar in chemical composition to the bone; in other words, they are identical in contrast in radiographic images;[22] therefore, the information obtained from these images is limited.[24] Several attempts have been made to increase the radiopacity of bioactive glasses by doping them with radiopacifiers. However, according to the results of these studies, many of these materials are toxic to biological tissues and reduce the bioactivity of the glasses.[22] Therefore, in addition to radiography, other non-invasive and non-destructive methods are also used to monitor the behavior of the implanted BAG.[23,24] One such method is NIR optical imaging, which is relatively new but promising and has significant potential for BAG imaging *in vivo*.[25–27]

1.3 Near-infrared (NIR) optical imaging

Over the past decades, optical imaging has become one of the most relevant and promising methods of *in vivo* imaging based on the interaction of light with biological tissues within the body.[28] The advantages of this method are non-invasiveness, high sensitivity, real-time imaging without the use of ionizing radiation, relative ease of implementation, the ability to combine with other imaging methods, and a wide selection of fluorophores and phosphors with different luminescence properties.[28,29] During the optical imaging, light penetrates the biological tissues of the body to excite luminescent substances, the emission of which then passes through the tissues and is read by a detector.[29] Interacting with the biological system, the intensity of the light signal weakens and limits the depth of light penetration, because it encounters such photophysical processes as reflection, scattering, and absorption. Additionally, some biomolecules convert the energy obtained from the absorption of radiation into an emission called autofluorescence, which negatively affects the contrast and resolution of the images.[30]

Traditionally, optical imaging has relied on ultraviolet (UV) and visible light, which are most susceptible to photophysical processes, and thus, they limit the penetration depth to approximately

one millimeter.[31,32] However, with the development of science and a better understanding of the processes of light-tissue interactions, researchers have concluded that in the NIR region (700−1700 nm) both absorption and scattering of light by biomolecules are significantly reduced and autofluorescence background is minimal, thereby increasing the depth of light penetration from millimeters to centimeters and enhancing images contrast.[33] In NIR imaging, the near-infrared region is divided into two "biological windows": the biological window I (NIR-I region, 700−950 nm) and the biological window II (NIR-II region, 1000−1700 nm), each of which has its own advantages. However, the light of the NIR-II region is the most promising for *in vivo* imaging because it has better properties.[34]

One of the important factors affecting image quality is the optical and chemical properties of contrast agents, which are typically injected into the body before optical imaging. Thus, fluorophores for NIR optical imaging must be biocompatible, low-toxicity, photostable, with a high quantum yield, and a large Stokes shift. They must also have intense and tunable luminescence properties in the NIR region.[28] Typical examples of contrast agents are organic molecule dyes[35], IR fluorescent proteins[36], quantum dots[37], single-walled carbon nanotubes[38], and nanophosphors[39]. In NIR optical imaging, narrow-band laser diodes (LDs) and high-energy light-emitting diodes (LEDs) are used as light sources to excite contrast agents, the emission of which is read by detectors such as CCD (charge-coupled device), InGaAs, and HgCdTe cameras.[40,41]

Nowadays, there are various optical imaging techniques that are based on certain optical properties of contrast agents used during imaging.[28] The most commonly used imaging techniques are bioluminescence imaging[42], chemiluminescence imaging[43], fluorescence imaging[44], persistent luminescence (PeL) imaging[45], and X-ray excited luminescence imaging[46]. The last three techniques are the most promising for this work because the contrast agent must be thermally stable when doped into a glass matrix (i.e., not destroyed at temperatures of 1000 °C or even higher).

For NIR fluorescence imaging, contrast agents with fluorescent properties are used. They are able to absorb NIR light of a particular wavelength and emit light of a longer wavelength.[44] In modern medicine, this technique is often used in diagnostics, treatment, and image-guided surgeries.[28,47]

Phosphors with NIR PeL properties are most commonly used in bioimaging and tumor imaging.[45,48] NIR PeL imaging is based on the ability of phosphors to continue to emit NIR light for an extended period (from minutes to hours) after the excitation source has been removed, which allows avoiding the autofluorescence of biological molecules and obtaining high-contrast imaging of deep biological tissues.[28]

X-ray excited NIR luminescence imaging uses luminophores that exhibit luminescence properties under X-ray excitation. In general, X-rays have much higher energy than non-ionizing radiation and can easily and deeply penetrate biological tissues without significant interaction with them. Therefore, using the advantages of this technique, it is possible to achieve high-quality, high-contrast, deep-tissue *in vivo* imaging.[28] This technique demonstrates the most promising results in bioimaging.[49]

All previously described NIR optical imaging techniques demonstrate high potential for safe, non-invasive, real-time monitoring of the implant's state in the host body. Unlike traditional approaches, in this research project, phosphors are doped into the structure of bioactive glasses or 3D scaffolds, modifying them into so-called biophotonic implants. Although only a few studies have been published on this topic so far, the preliminary results indicate the promising potential of biophotonic implants in regenerative medicine.[27,50–54]

1.4 Biophotonic BAGs

Examples of successful doping of PeL phosphors into the glass structure were demonstrated by Nakanishi et al. and Massera et al. about 10 years ago.[50,51,54] Thus, Nakanishi et al. fabricated alumino-borate glass with PeL properties by doping the glass structure with $SrAl_2O_4:Eu^{2+},Dy^{3+}$ phosphor using the frozen sorbet method. The obtained glass composites showed a greenish-yellow PeL emission with a maximum at 520 nm after irradiation with 393 nm light.[54] Building upon this foundation, Massera et al. successfully doped a phosphate-based BAG with $SrAl_2O_4:Eu^{2+},Dy^{3+,}$ and $CaAl_2O_4:Eu^{2+},Nd^{3+}$ phosphors using the glass melting method. The results indicated that the synthesized glasses exhibit PeL properties after irradiation with UV light (254 nm). Thus, BAG containing $SrAl_2O_4$ phosphor particles showed two emission bands at 410 and 490 nm, whereas BAG composite with $CaAl_2O_4$ particles exhibited only one broad band with a maximum at 445 nm.[50,51] Later, Saarinen et al. successfully prepared phosphate and borosilicate BAGs containing $SrAl_2O_4:Eu^{2+},Dy^{3+}$ by sintering glass particles with PeL phosphor. Both types of BAGs showed a PeL emission at 410 and 490 nm after irradiation with 254 nm light. It was also observed that the optical properties of the glass decreased during the formation of the HA layer, which probably absorbs white light. Therefore, this biomaterial could potentially be used as a biophotonic sensor for monitoring biomineralization.[52]

Despite the promising results demonstrated in the above studies, the use of such biophotonic materials in NIR optical imaging is limited because their optical properties are exhibited in the UV and visible light regions. However, several more recent studies have been published that describe the NIR optical properties of glass composites.[27,53]

In 2023, Zhang et al. developed upconversion mesoporous BAG microspheres doped with Er^{3+} and Yb^{3+} ions. This upconverted luminescence biomaterial showed two emission bands in the green (540−570 nm) and NIR-I (650−725 nm) regions under excitation of NIR light with a wavelength of 980 nm. According to the results, MBAG:Er/Yb microspheres demonstrated potential for biomineralization monitoring and optical imaging applications.[53]

Later, in 2024, Xu et al. synthesized a bioceramic material, $CaTiO_3$, doped with Cr^{3+} and Y^{3+} ions (CTCY). The material showed NIR PeL emission with a maximum at 772 nm after red light (650 nm) excitation. During this study, the CTCY powder was mixed with polylactic acid to prepare a bone screw, which then was implanted into a pig forelimb for *in vivo* optical imaging. Based on the results, the PeL signal could still be detected when the tissue thickness was 17 mm. Therefore, this type of biophotonic implant demonstrated promising results in NIR optical imaging.[27]

1.5 NIR phosphors

NIR phosphors are inorganic materials that exhibit luminescence properties in the NIR region. In general, phosphors consist of an host material (host lattice) and activator ions that are doped into it.[55] Typical examples of host materials are oxides, aluminates, sulfides, fluorides, silicates, germanates, and titanates. Transition metal ions (Cr^{3+}, Cr^{4+}, Mn^{4+}, Mn^{2+}, Ni^{2+}) and rare earth ions (Eu^{3+}, Yb^{3+}, Nd^{3+}, Er^{3+}, Ho^{3+}, Eu^{2+}, Tm^{3+}) are most often used as NIR activators, since their luminescence properties have been well studied.[56,57] Moreover, impurities and intrinsic defects of the host matrix can also act as activators, causing luminescence properties in undoped material.[55] Compared with organic contrast agents and other luminophores, phosphors have many significant advantages, such as bright tunable emission, photostability, large Stokes shift, high quantum yield, thermal and chemical stability, and long luminescence lifetime.[58]

One of the promising NIR phosphor hosts is MgO, which has a simple cubic lattice structure and is easily synthesized by various synthesis methods.[56,59] This host material has a wide band gap (7.8 eV), which allows the creation of many variations of MgO phosphor with different luminescence and trapping centers depending on the doped ions.[60] Moreover, it is non-toxic at low concentrations and has high chemical and thermal stability.[61] Since MgO contains impurities and many intrinsic defects, it has various luminescence properties, such as thermoluminescence (TL), photoluminescence (PL), optically stimulated luminescence (OSL), and radioluminescence (RL).[62,63] Therefore, this phosphor has been intensively studied over the past decades for its potential application in TL dosimetry.[59]

Additionally, numerous studies have been conducted on doping MgO with rare earth and transition metal ions to modify and improve the optical properties of the material. Red and NIR emissions have

been observed in samples doped with ions such as Sm^{3+}, Eu^{3+}, Cr^{3+}, and Er^{3+}.[56,61,64,65] Moreover, the OSL, TL, PeL, and RL properties in the red range were observed in MgO phosphor doped with three different ions: Ce^{3+}, Sm^{3+}, and Li^{+}.[60] It was found that the presence of Li^{+} ions significantly improved the intensity of emissions since they created negatively charged defects in the host material, acting as charge compensators.[61] It was also noted that the luminescence centers formed due to Li^{+} doping facilitate the energy transfer between them and the luminescence centers of trivalent ions.[66]

Another promising NIR phosphor host is magnesium germanate ($Mg_{14}Ge_5O_{24}$), which has an olivine structure and a 5.8 eV band gap.[67] This phosphor, doped with lanthanide and transition metal ions, demonstrated luminescence properties in the NIR region.[67,68] Thus, it was found that doping with Cr ions leads to the appearance of broad PL emission bands in both NIR-I and NIR-II regions under UV and NIR (NIR-II emission) light excitation.[67]

The phosphors synthesized in this work were based on the two above-mentioned host materials.

1.6 The background and aims of this work

Over the past decades, many types of third-generation biomaterials have been successfully developed; however, there has been a growing interest in creating new fourth-generation biomaterials that are capable of not only stimulating the regeneration of native tissue by gradually biodegrading but also have properties that facilitate non-invasive postoperative monitoring. Therefore, the development of biophotonic BAGs with NIR optical properties is especially relevant because it enables the application of several *in vivo* imaging techniques for real-time monitoring of implanted BAGs. Thus, today, the main challenge for researchers is the development and fabrication of NIR phosphors with desired optical properties, such as OSL, XEOL, PeL, and PL. One promising candidate for this purpose is MgO-based phosphors, which exhibit high biocompatibility, thermal stability, and NIR optical properties.

Therefore, the aims of this work are to improve the NIR optical properties of MgO- and MGO-based phosphors by doping them with selected ions and varying the dopants concentration in the host material; to fabricate glass-phosphor composites by doping the samples with the best optical properties into the glass matrix and 3D-printed scaffolds; and finally, to compare the NIR optical properties of the obtained composites with the original phosphors in order to assess their potential for NIR imaging applications.

The results of this work may represent another step towards the development of a new generation of BAGs that integrate therapeutic and diagnostic functions within a single biomaterial.

2. Experimental section

Doped MgO with Li^+, Ce^{3+}, Sm^{3+} ions was synthesized by the solution combustion synthesis (SCS) method, which was described by Oliveira et al.[60] SCS is one of the types of self-propagating high-temperature synthesis. Usually, to generate a combustion reaction, four components are required: an oxidizer (metal nitrates), an organic fuel (urea), a solvent (distilled water), and a high temperature (500 °C).[69]

$Mg_{14}Ge_5O_{24}$ (MGO) material was synthesized using the high-temperature solid-state method as described earlier by Wang et al.[34] The material was doped with such ions as Cr^{3+}, Mn^{4+}, Yb^{3+}, Ho^{3+}, Nd^{3+}, and Tm^{3+}.

The glass-phosphor composites were fabricated using three different techniques: remelting, the direct doping method (DDM), and the so-called sandwich method. The glass with the $50P_2O_5$-40SrO-$10Na_2O$ composition was doped with selected phosphor samples, which showed the best optical properties in the NIR region. Besides, the 3D-printed scaffolds with the $45P_2O_5$-$2.5B_2O_3$-$2.5SiO_2$-$10Na_2O$-20CaO-10SrO-10MgO composition were also doped with the best powder samples. A detailed description of the fabrication techniques for the glass-phosphor composites and doped 3D scaffolds is provided in the supporting information (**Table S1**).

2.1 Synthesis of MgO:$Li_{x\%}Ce_{y\%}Sm_{z\%}$

The starting materials for solution combustion synthesis included magnesium nitrate hexahydrate ($Mg(NO_3)_2 \cdot 6H_2O$, Merck, 99%), urea ($CO(NH_2)_2$, Sigma Aldrich, 98%), lithium nitrate ($LiNO_3$, J.T.Baker, 97%), cerium nitrate hexahydrate ($Ce(NO_3)_3 \cdot 6H_2O$, Sigma Aldrich, 99%) and samarium oxide (Sm_2O_3, Typpi Oy, 99%). Aqueous solutions were prepared from all mentioned chemicals, with concentrations listed in the same order as above: 2 M, 8.33 M, 1.5 M, 0.015 M, and 0.015 M. Samarium nitrate ($Sm(NO_3)_3$) solution was prepared by dissolving Sm_2O_3 in nitric acid 65% (Merck). Initially, undoped MgO was synthesized as a reference sample. At first, 25 ml of $Mg(NO_3)_2$ solution was mixed with 10 ml of urea solution in a glass beaker. The mixture was stirred for several minutes and then heated on a hot plate at approximately 200 °C for about one hour until complete evaporation of water occurred. After that, the resulting gel-like mass was transferred into an alumina crucible and placed in a preheated Nabertherm N3/C8 furnace at 500 °C. The crucible was kept in the furnace for 8-10 minutes, until a combustion reaction occurred, releasing greenish-brown gas and flame. As a result, a solid white paste was obtained, which was then ground in an agate mortar. The white powder was transferred into an alumina boat crucible and placed in a Carbolite Gero EST 12/600B furnace for annealing at 900 °C for 2 hours, with a heating rate of 5 °C/min in an open atmosphere. After that, the obtained powder was ground again.

Other doped MgO samples were synthesized in the same way. However, the specific volumes of lithium, samarium, cerium nitrate solutions were also added to the main mixture, depending on the desired concentration of dopants in each sample. The dopant concentrations were calculated as mol-% relative to the amount of Mg. Accordingly, for lithium ions ($Li_{x\%}$), x = 0, 3, 6, 9, 12, and 24%; for cerium ions ($Ce_{y\%}$), y = 0.03, 0.06, 0.12, and 0.24%; and for samarium ions ($Sm_{z\%}$), z = 0.03, 0.06, 0.12, and 0.24%. The full list of synthesized samples is provided in the supporting information (**Table S2**).

2.2 Synthesis of doped MGO

The starting materials used in the solid-state synthesis were magnesium carbonate ($MgCO_3$, Merck, >99%), germanium oxide (GeO_2, Sigma Aldrich, >99%), chromium oxide (Cr_2O_3, Sigma Aldrich, 99%), manganese dioxide (MnO_2), and ytterbium, neodymium, thulium, holmium oxides (Yb_2O_3, Nd_2O_3, Tm_2O_3, Ho_2O_3). MgO was prepared by the calcination of $MgCO_3$ at 1000 °C.

The undoped MGO sample was synthesized as a reference sample. To prepare 1 g of the material, 0.519 g of MgO and 0.481 g of GeO_2 were weighed and ground in the agate mortar for 15 minutes. After that, the powder mixture was transferred to alumina boat crucible and placed into a Big Elite TSH15/50/450-2416CG furnace for sintering at 1350 °C for 4 hours, with a heating rate of 3 °C/min in air. After cooling, the sample was ground again in the mortar.

All samples were synthesized using the same process, which included the addition of oxides containing dopant ions to the main mixture. The dopant concentrations were calculated as mol-% relative to the amount of MGO substance. Thus, for MGO:$Cr_{x\%}$ batch, x = 1, 3, 5, 7, 10, 13, 16, and 19%; for MGO:$Cr_{10\%}$, $Mn_{x\%}$ batch, x = 0.5, 0.75, 1, 1.5, and 2%; for MGO:$Cr_{10\%}$, $Ln_{x\%}$, (Ln = Nd, Tm, Ho) batches, x = 1, 3, 5, 7, 9, and 11%; for MGO:$Cr_{7\%}$, $Mn_{0.5\%}$, $Yb_{x\%}$ batch, x = 1, 3, 5, 7, 9%. The samples from the first two batches are listed in the supporting information (**Table S3**).

2.3 Characterization methods

Powder X-ray diffraction (PXRD)

The X-ray diffraction patterns of the obtained powder samples were measured using a PANalytical Aeris diffractometer equipped with a copper (Cu) X-ray tube and PIXcel1D-Medipix3 detector. The measurements were performed with Cu Kα radiation ($K\alpha_1$ = 1.5406 Å and $K\alpha_2$ = 1.5444 Å) at 40 kV and 7.5 mA, with a step size of 0.0217°. The instrument setting included a Ni beta-filter, 0.04 rad Soller slits, a 13 mm mask, a 1/4° divergence slit, a 9 mm AS slit, and a beam knife in the high position.

The phase identification was performed using PANalytical HighScore Plus software, which compared the experimental diffraction patterns with reference patterns from the ICDD PDF-4+ database to determine phase compositions of the samples.

X-ray fluorescence (XRF)

The elemental composition of the synthesized samples was analyzed using a PANalytical Epsilon 1 XRF spectrometer with an Ag X-ray tube. XRF measurements were conducted using the "Na 1h without the first step" program, which consists of three measurement cycles with different setting parameters (as listed in **Table 1**). The results of all measured samples were collected in **Tables S2** and **S3** in the supporting information.

Table 1. The parameters of each measurement cycle of the "Na 1h without the first step" program.

Measurement	Acceleration voltage (kV)	Filter	Detector mode	Measurement time (s)	Measurement range (eV)
1	50	Cu (500 μm)	normal	300	2−34
2	12	Al (500 μm)	high	180	automatic
3	10	-	high	3000	0.9−4

Photoluminescence (PL)

The photoluminescence properties of the obtained samples were measured using a Varian Cary Eclipse Fluorescence Spectrophotometer with a 150 W xenon lamp and a Hamamatsu R928 photomultiplier tube. The PL spectra were measured in fluorescence mode using the following parameters: gate time of 5.0 ms, delay time of 0.1 ms, excitation slit width of 10 nm, emission slit width of 5 nm for MgO samples and 2.5 nm for MGO samples, and a step size of 0.2 nm. Depending on the samples, the detector voltage varied from 600 V to 800 V.

The PL spectra in the NIR region were recorded using an Avantes AvaSpec NIR 1.7 CCD spectrometer connected to the Avantes FC-UVIR600-1 optical fibre. The measurements were performed in high-sensitivity mode for 900 ms. A LOT-QuantumDesign MSH300 monochromator and a LOT-QuantumDesign LSB522 150 W xenon lamp were used as the excitation source.

The PL spectra of glass-phosphor composites were measured using an Edinburgh Instruments FLS1000 Luminescence Spectrometer.

Thermoluminescence (TL)

The TL glow curves of undoped and doped MgO samples were recorded using a MikroLab Thermoluminescent Materials Laboratory Reader RA'04 at a heating rate of 10 °Cs^{-1}. Before measurements, the samples were irradiated with X-rays from the PANalytical Epsilon 1 device for 26 minutes. Several samples synthesized earlier were irradiated with X-rays for 40 or 60 minutes because this was the initial irradiation time, which was later shortened to save measurement time. The same approach was used to investigate the TL property of the crushed 3D-printed scaffold doped with MgO phosphor.

Optically stimulated luminescence (OSL)

To determine whether the synthesized doped MgO material exhibited OSL properties, a series of experiments was conducted using a Canon EOS 250D camera (with a glass filter Standa C3C-24), a PANalytical Epsilon 1 device (for X-ray irradiation), and a Roithner LaserTechnik RLTMFC-980-50W-1 laser with 980 nm wavelength (for laser stimulation). The distance between the laser and the samples was 11 cm, the laser power was 5.5 W, and the X-ray irradiation dose delivered to the samples was approximately 51 mSv (0.051 Gy). For each selected sample, four photographs were taken in a dark room: (1) the sample in darkness, (2) the sample under laser stimulation, (3) the sample after 20 minutes of X-ray irradiation, and (4) the X-ray pre-irradiated sample under laser stimulation. The emission in the fourth photograph indicates the presence of the OSL property in the material. Additionally, to eliminate the possibility of TL emission that may occur due to heating the samples to 85 °C during laser stimulation, a couple of samples were cooled with liquid nitrogen (−195.8 °C) and dry ice (−78.5 °C) during the experiment.

The same experimental approach was used to assess the OSL properties of both the glass-phosphor composites and the doped 3D scaffolds.

Cathodoluminescence (CL) and persistent luminescence (PeL)

To investigate the CL properties of the materials, CL emission spectra were recorded. A Nuclide Corporation ELM2EX Luminoscope equipped with a Nuclide Corporation ELM2B vacuum chamber was used to bombard the samples with a 12.5 keV electron beam. The CL emission spectra were collected using an Avantes AvaSpec HS-TEC CCD spectrometer in the 180−1100 nm region and an Avantes AvaSpec NIR 1.7 CCD spectrometer in the 800−1700 nm region. The Avantes FC-UV600-1-SR and FC-UVIR600-1 optical fibres connected to the CCD spectrometers were used to conduct the measurements.

PeL spectra were collected using the Avantes AvaSpec HS-TEC CCD spectrometer. The samples were bombarded with a 12.5 keV electron beam for 40 s, and the PeL emission was recorded immediately after the beam was turned off.

Photographs of the samples' emission under the electron beam and after stopping the irradiation were taken using a Canon EOS 250D camera in a dark room.

3. Results and discussion

During this research project, two different phosphor materials with luminescence properties in the NIR region were synthesized. Then, the optical properties of all synthesized samples were measured, and based on the obtained results, the best samples were selected for doping into a glass matrix. After that, the optical properties of the fabricated glass-phosphor composites were compared with the properties of the original phosphors.

3.1 MgO phosphor

During the first part of the work, MgO samples doped with different concentrations of Ce^{3+}, Sm^{3+}, and Li^{+} ions were synthesized. Then, XRD, XRF, PL, OSL, CL, and PeL properties were measured for all samples.

X-ray diffraction patterns were measured for all synthesized samples to determine and identify their phase composition using the ICDD PDF-4+ reference database. All measured XRD patterns are shown in **Figure 1**. The diffractograms of the undoped sample and samples with low dopants concentrations (0.03−0.06% of Ce^{3+} and Sm^{3+} ions) show the presence of a single MgO phase (01-076-6597), with characteristic reflections at $2\theta \approx 36.58°$, 42.63°, 62.01°, 74.39°, and 78.38°. However, in the diffraction patterns of samples with a higher lanthanide ions concentration (≥ 0.12%), the presence of two different phases is noticeable. One of these phases is MgO (01-076-6597), and the other, according to the database, is CeO_2 (04-013-4461). Compared to the main MgO phase, the intensity of the impurity phase is very low with reflections at $2\theta \approx 28.20°$, 32.70°, 46.98°, and 55.72°.

Therefore, it can be concluded that the solution combustion synthesis of both undoped and doped MgO was successful, and the desired material was obtained. The dopant ions were successfully incorporated into the host lattice, which can also be confirmed by the results obtained from XRF measurements (**Table S2**). The appearance of the CeO_2 phase indicates that the “solubility” limit of cerium in the MgO lattice was exceeded, leading to the formation of the impurity phase. This can be confirmed by the publication of Matsukevich et al., which describes the process of preparing mesoporous nanocomposites based on CeO_2 and MgO using self-propagating high-temperature

synthesis.[70] Additionally, in some XRD patterns, a slight shift of the most intense reflection at 42.63° can be observed, which may indicate a slight change in the lattice parameters due to doping ions.

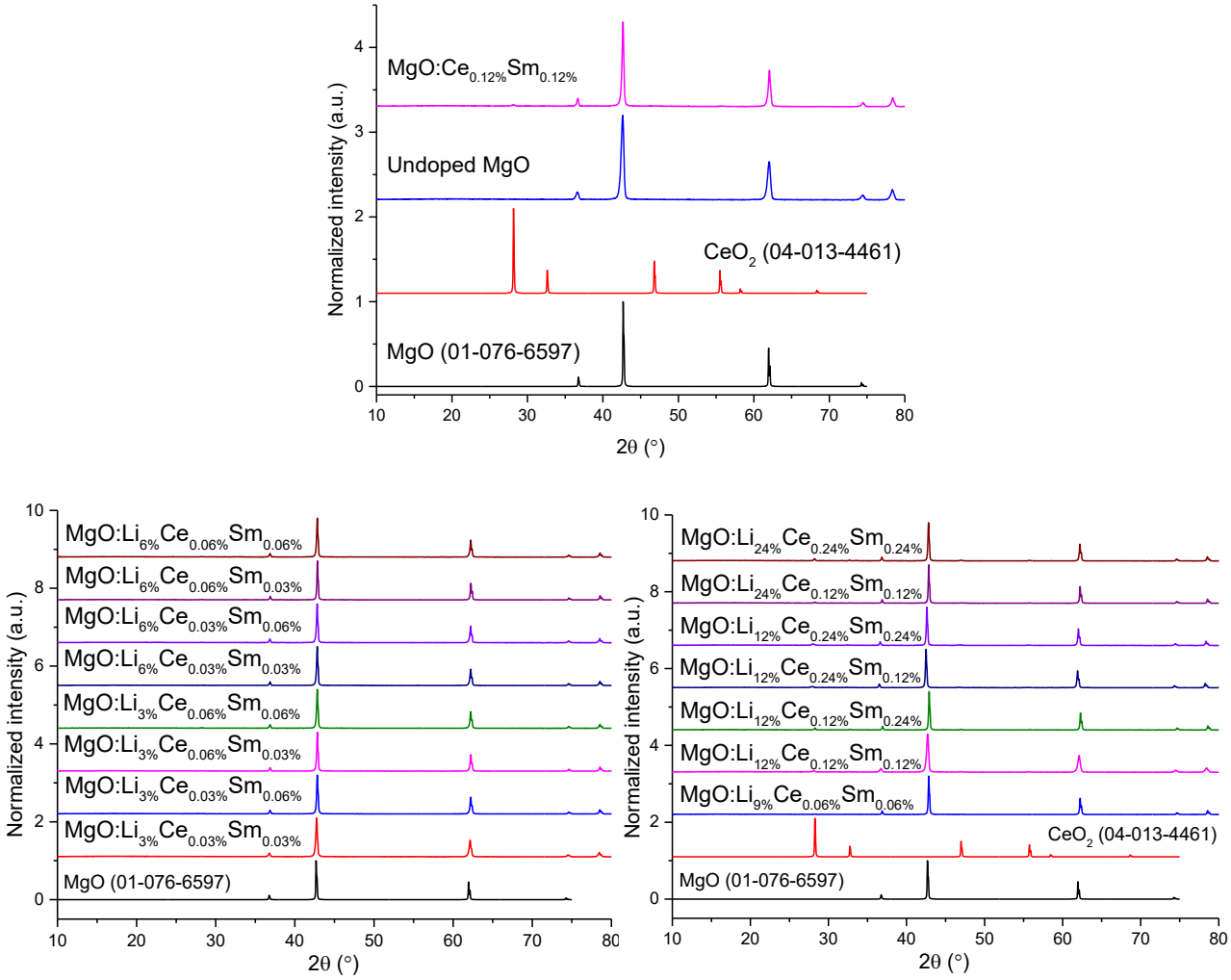

Figure 1. XRD patterns of the obtained samples.

To assess the trap properties of the phosphor, TL glow curves were measured for all obtained samples (**Figure 2**). Most samples were pre-irradiated with X-rays for 26 min. However, the MgO, $MgO:Ce_{0.12\%}Sm_{0.12\%}$, $MgO:Li_{12\%}Ce_{0.12\%}Sm_{0.12\%}$, $MgO:Li_{12\%}Ce_{0.24\%}Sm_{0.12\%}$, and $MgO:Li_{12\%}Ce_{0.24\%}Sm_{0.24\%}$ samples were irradiated for either 40 or 60 min because they had been synthesized earlier than the others, and different TL measurement parameters were used at that time.

From **Figure 2**, it is noticeable that the TL glow curve of the undoped MgO exhibits two weak TL emission peaks with maxima at 190 and 360 °C, which indicates the presence of two types of traps with different depths. The TL emission at 190 °C can be explained by the presence of intrinsic defects in the MgO lattice, whereas the deeper traps (TL emission at 360 °C) are probably due to the tiny amount of impurities in the sample.[63] It is also noticeable that the doped MgO with Ce^{3+} and Sm^{3+} ions exhibits two TL glow peaks at 220 and 285 °C with relatively low intensity. The fact that the

second glow peak is twice as intense as the first indicates that lanthanide doping forms many deeper traps due to substitutional defects in the MgO lattice.[61] It was also determined that doping Li^+ ions together with lanthanide ions significantly affects the intensity of the TL glow peak at high temperatures (250−350 °C). With an increase in the concentration of Li^+ ions from 3% to 12%, the intensity of the TL glow peak also increases, except for the samples that were synthesized earlier (listed above). This can be explained by the fact that the negative charge defect formed by Li^+ ions in the host lattice facilitates the doping of trivalent lanthanide ions into the structure of the material.[61] It is also noticeable that at 24% Li^+, the TL glow intensity remains relatively high but does not prevail over the sample containing 12% Li^+. The effect of different concentrations of lanthanide ions on the TL glow curves was not noticed. Thus, the sample with the most intense TL glow peak at 298 °C is $MgO:Li_{12\%}Ce_{0.12\%}Sm_{0.24\%}$. This sample, as well as $MgO:Li_{24\%}Ce_{0.12\%}Sm_{0.12\%}$, $MgO:Li_{24\%}Ce_{0.24\%}Sm_{0.24\%}$, and $MgO:Li_{6\%}Ce_{0.03\%}Sm_{0.06\%}$ samples, are promising candidates for OSL, since the obtained TL results indicate a high density of deep traps with an activation energy sufficient to accumulate and hold electrons until external optical stimulation.[60]

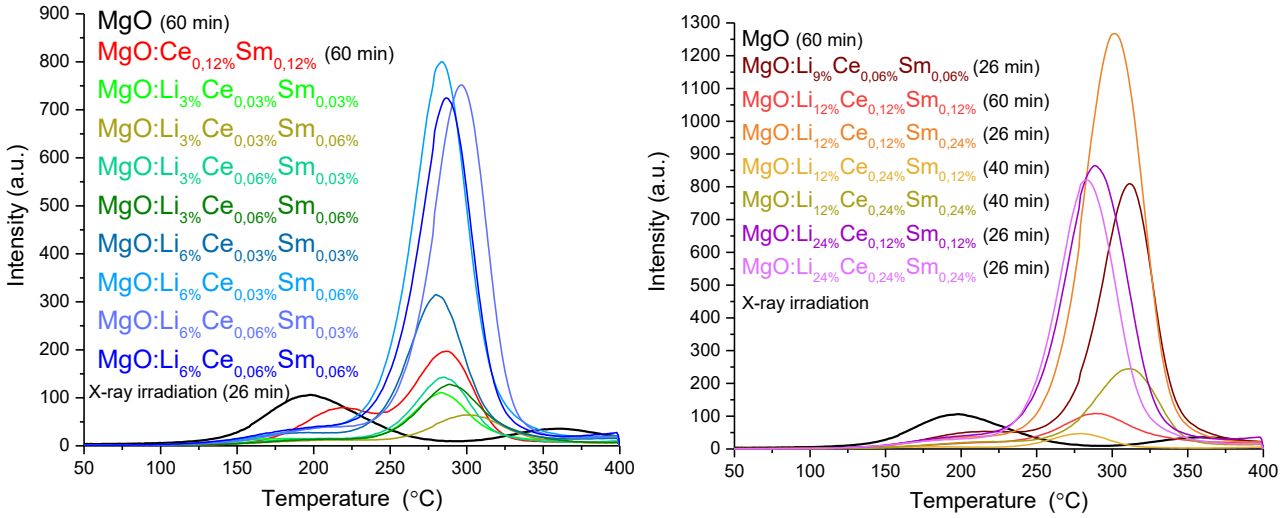

Figure 2. TL glow curves of the synthesized samples.

To confirm the presence of the OSL property of the material, three samples ($MgO:Li_{12\%}Ce_{0.12\%}Sm_{0.24\%}$, $MgO:Li_{24\%}Ce_{0.12\%}Sm_{0.12\%}$, $MgO:Li_{24\%}Ce_{0.24\%}Sm_{0.24\%}$) with the best TL properties and one sample ($MgO:Li_{3\%}Ce_{0.03\%}Sm_{0.03\%}$) with a weak TL glow were selected. Since we did not have a device for measuring OSL, a Canon EOS 250D camera and a laser with a wavelength of 980 nm were used to detect this property. For more convincing results, five photographs of each sample were taken under different photographic conditions, but with the same camera settings (aperture f/0, exposure time 30 s, ISO-6400, shutter-priority exposure mode, and automatic white balance). All the photographs are shown in **Figure 3**.

In the photographs of the first three columns, no emission was recorded; they are entirely black. However, they were taken under different conditions, the photos in the first column were taken in complete darkness without any excitation, while the samples in the second column were excited to a 980 nm laser during photography, and the photos of the third column show the samples after 20 minutes of preliminary irradiation with X-rays. This indicates that the samples do not exhibit visible emission under 980 nm laser excitation, and do not show long-lasting PeL after irradiation with X-rays. The photographs in the fourth column show visible emission, which is most likely caused by optical stimulation because during the photography the samples, which had been previously irradiated with X-rays, were stimulated by the laser. Thus, the MgO:$Li_{3\%}Ce_{0.03\%}Sm_{0.03\%}$ sample shows a reddish, weak glow, while the other samples exhibit a bright white emission. The photos in the fifth column show samples under room lighting.

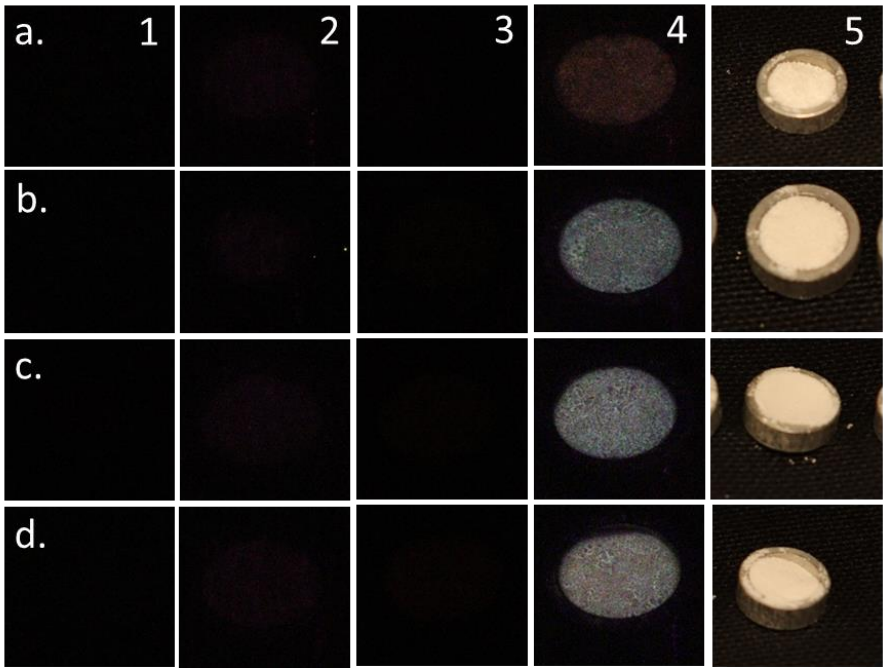

Figure 3. Row a: MgO:$Li_{3\%}Ce_{0.03\%}Sm_{0.03\%}$; row b: MgO:$Li_{12\%}Ce_{0.12\%}Sm_{0.24\%}$; row c: MgO:$Li_{24\%}Ce_{0.12\%}Sm_{0.12\%}$; row d: MgO:$Li_{24\%}Ce_{0.24\%}Sm_{0.24\%}$. Column 1: photographs of samples in the dark; column 2: photographs of samples under laser stimulation; column 3: photographs of samples in the dark after X-ray irradiation; column 4: photographs of samples under laser stimulation, after X-ray irradiation; column 5: photographs of samples under room lighting.

In order to exclude the possibility of TL glow occurrence due to heating of the sample by the laser beam to approximately 85 °C during stimulation, it was decided to repeat the experiment using liquid nitrogen (−195.8 °C) as a coolant. The sample was placed in a container with liquid nitrogen (other stages of the experiment remained the same). However, due to its intense boiling at room temperature and evaporation in the form of gas, it was difficult to obtain a clear photograph of the sample during laser stimulation. Therefore, the experiment was repeated using dry ice (solid carbon dioxide, −78 °C).

The photos (**Figure 4**) of the MgO:$Li_{3\%}Ce_{0.06\%}Sm_{0.06\%}$ sample were taken under the same conditions as the photographs of the samples above and are arranged here in the same order. Photographs **2**, **4(1)**, and **4(2)** show a purple glow coming from the laser beam because the camera settings were slightly adjusted for this experiment (aperture f/0, exposure time 30 s, ISO-6400, manual exposure mode, and manual white balance). The reflected NIR radiation from the laser looks purple, because the camera's blue and red pixels also detect NIR. In photographs **4(1)** and **4(2)**, the emission of the sample is noticeable, which confirms that the synthesized samples have OSL properties. It is also interesting that at different ISO values but under identical photographic conditions and parameters, two different emissions are noticeable: at ISO-6400 (**4(1)**) white, and at ISO-800 (**4(2)**) orange. In theory, this can be explained by the fact that at ISO-6400, the camera matrix significantly amplifies both the "desired" photo signal and noise. Therefore, the orange glow could be "lost" against the background of noise and looks like a distorted, discolored white glow in the photo. However, when the sensitivity is reduced to ISO-800, it is easier for the matrix to capture and correctly convey the actual shade of the orange glow.[83–85] Thus, it is possible that by lowering the ISO value, the photographs of the samples in **Figure 3** would also show a more reddish-orange emission. To prove or disprove that, the experiment must be repeated.

An attempt to measure the OSL emission spectra was also made, but it was unsuccessful. However, based on the OSL emission spectrum recorded by Oliveira et al.[60], which was obtained by scanning a MgO:LiCeSm sample during stimulation with 700 nm light after its preliminary irradiation with 30 Gy X-rays, it can be assumed that white OSL emission may indeed appear depending on the intensity of the emission bands. Since the emission spectrum consists of two broad emission bands with maxima at 480 nm and 517 nm, and four narrow, sharp emissions at approximately 574, 583, 610, and 627 nm.

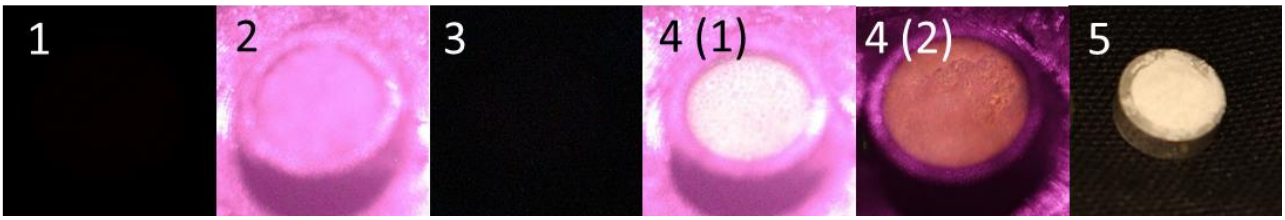

Figure 4. MgO:$Li_{3\%}Ce_{0.06\%}Sm_{0.06\%}$ sample. 1: in the dark room, 2: under laser stimulation, 3: in the dark after X-ray irradiation, 4(1): under laser, after X-ray irradiation, ISO-6400, 4(2): under laser, after X-ray irradiation, ISO-800, 5: under room lighting.

PL emission spectra of all synthesized samples were recorded under both 254 nm and 450 nm excitation. **Figure 5** shows the PL emission spectra of selected samples for ease of interpretation, since for most samples the emission maxima and their intensity coincide. The excitation spectra of

the presented samples are provided in the supporting information (**Figure S1**). Thus, the undoped MgO shows weak emission at 680 nm under 254 nm excitation and a broad, weak emission band with two maxima at 700 and 721 nm under 450 nm light excitation. At the same time, the MgO:$Ce_{0.12\%}Sm_{0.12\%}$ sample exhibits a weak emission in the 550−650 nm range under 254 nm excitation, as well as a relatively intense broad emission band of 650−800 nm with two narrow emission peaks at 700 and 721 nm and three more maxima at 680, 690 and 712 nm, excited by 450 nm light. It is noticeable that the addition of Li^+ ions into the MgO host material significantly increases the emission intensity in the 550−700 nm range under 254 nm excitation but does not affect the emission in the 650−800 nm range, excited by 450 nm light. Upon excitation at 254 nm, the doped samples exhibit intense emission bands with maxima at 577, 590, 611, 625, 655, 669, 681, 701, and 721 nm. It is also noticeable that increasing the amount of Ce^{3+} and Sm^{3+} ions leads to an increase in the emission intensity at 450 nm excitation. The discussion of the results is described at the end of this chapter.

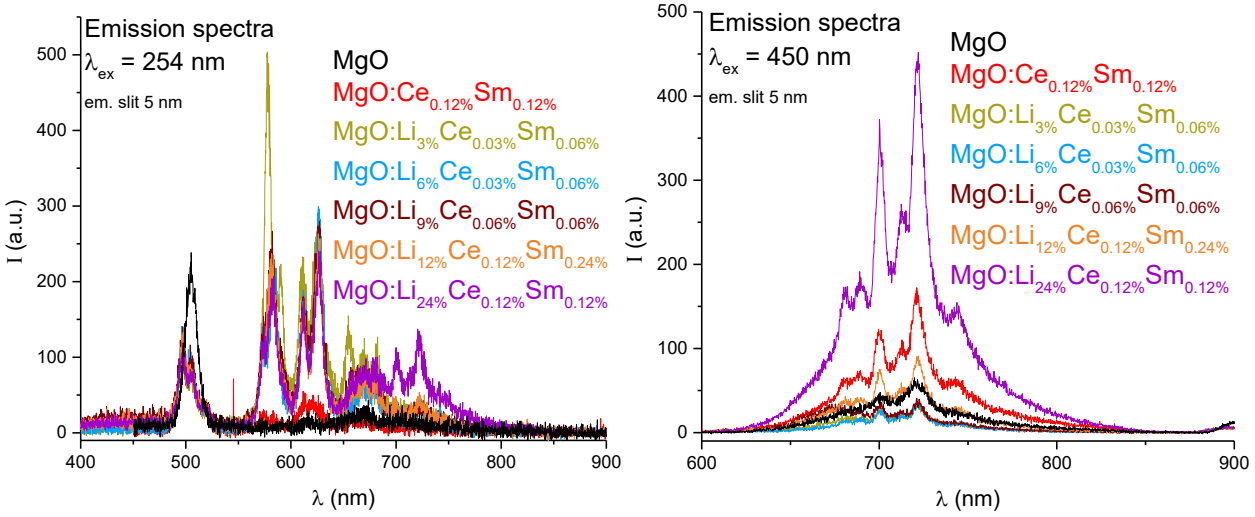

Figure 5. PL emission spectra for undoped and doped MgO samples (left: λ_{ex} = 254 nm; right: λ_{ex} = 450 nm).

All synthesized samples were measured for cathodoluminescence to assess the luminescence properties of the samples under high-energy electron beam excitation. This will allow us to determine whether the obtained material has the ability to X-ray excited optical luminescence (XEOL) because the energy of the electron beam is in the X-ray energy range. CL emission spectra are shown in **Figure 6**. It can be seen that under electron beam excitation, undoped MgO exhibits a weak emission at 740 nm and a broad emission band in the range from 1150 nm to 1550 nm, with a maximum at approximately 1300 nm. Whereas the MgO:$Ce_{0.12\%}Sm_{0.12\%}$ sample shows weak emission in the visible range from 550 nm to 700 nm with maxima at 583, 590, 618, 632 and 682 nm, as well as intense emission in the NIR region, namely narrow emission bands at 948, 1009, 1090 nm and one

broad emission band in the range from 1150 nm to 1550 nm. This may indicate that when the material is doped with lanthanide ions, emission bands appear in the ranges of 550−700 nm and 900−1100 nm. It is also noticeable that doping the material with both Li^+ and lanthanide ions greatly enhances the intensity of the emission bands in the 550−700 nm region and affects the appearance of an emission band in the range from 450 nm to 550 nm with a maximum at 527 nm.

Further, when comparing samples with different concentrations of Ce^{3+} ions, it was noted that the emission intensity in the range from 450 to 550 nm is significantly higher in those samples that contain a larger amount of Ce^{3+}. For example, the maximum emission intensity of the MgO:$Li_{3\%}$**$Ce_{0.03\%}$**$Sm_{0.06\%}$ sample is approximately 7000, while for the MgO:$Li_{3\%}$**$Ce_{0.06\%}$**$Sm_{0.06\%}$ sample it is around 23 000; for the MgO:$Li_{24\%}$**$Ce_{0.12\%}$**$Sm_{0.12\%}$ it is around 17 000, while for the MgO:$Li_{24\%}$**$Ce_{0.24\%}$**$Sm_{0.24\%}$ it is around 41 000. This may indicate that the emission band in this range can be attributed to the characteristic 5d→4f transition of the Ce^{3+} ion.

The same trend was observed for the emission bands in the range from 550 nm to 650 nm when comparing samples with different concentrations of Sm^{3+} ions. For example, the emission intensity of MgO:$Li_{3\%}Ce_{0.03\%}$**$Sm_{0.03\%}$** sample is approximately 24 000, while for MgO:$Li_{3\%}Ce_{0.03\%}$**$Sm_{0.06\%}$** it is approximately 37 500. In addition, it is noticeable that samples containing a larger amount of Sm^{3+} ions have more intense emissions in the NIR region, namely at 980, 1010, and 1084 nm. However, this trend is observed only for samples with a Li^+ ion concentration of 3−9%; for other samples, there is no correlation between concentration and intensity. Thus, these results may indicate that emissions in these ranges arise due to the presence of Sm^{3+} ions in the material.

Furthermore, it should be noted that the emission intensity in the 650−800 nm and 1200−1550 nm ranges does not depend on the concentration of dopants in the material. The discussion of the results is also described at the end of this chapter.

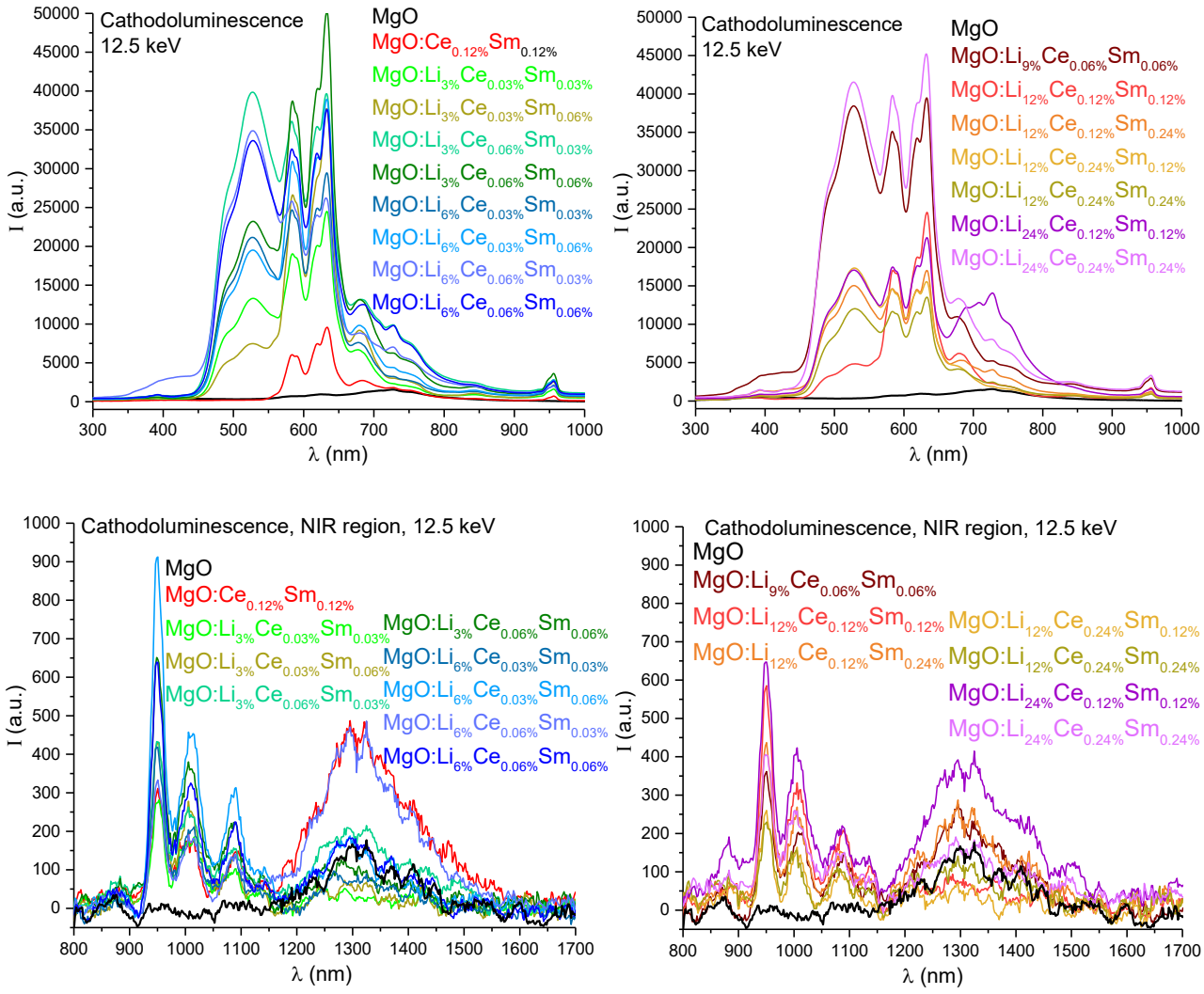

Figure 6. CL emission spectra under a 12.5 keV electron beam excitation. Upper emission spectra: visible range and NIR region; lower emission spectra: NIR region.

During the recording of the CL spectra, it was noticed that the doped samples had a red afterglow immediately after the electron beam was switched off. This indicated that the material had PeL properties after excitation by the electron beam. To confirm this fact the three photographs were taken (**Figure 7**). The first photograph (**a**) was taken in the dark, the second one (**b**) shows the samples under the electron beam, and the third (**c**) shows the samples immediately after the electron beam was switched off. In the second photograph (**b**), the visible emission of the samples coincides with the recorded CL spectra. Thus, undoped MgO in the photo exhibits a violet emission, which is attributed to the camera's perception and recording of NIR emission. The $MgO:Ce_{0.12\%}Sm_{0.12\%}$ and $MgO:Li_{3\%}Ce_{0.06\%}Sm_{0.06\%}$ samples show an orange glow, since their most intense emission bands are in the range from 600 to 650 nm. At the same time, the other samples have a white glow, since their emission bands are of approximately the same intensity and cover the entire visible range of the

spectra. It is also noticeable that in the last photo (**c**), a red PeL emission is observed only for the doped samples, while undoped MgO has no afterglow.

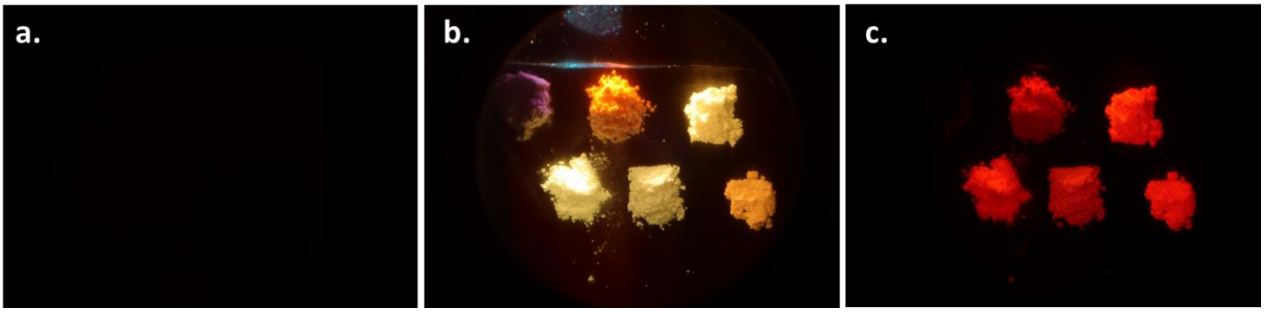

Figure 7. Photographs of samples MgO, MgO:$Ce_{0.12\%}Sm_{0.12\%}$, MgO:$Li_{6\%}Ce_{0.06\%}Sm_{0.06\%}$, MgO:$Li_{12\%}Ce_{0.12\%}Sm_{0.24\%}$, MgO:$Li_{9\%}Ce_{0.06\%}Sm_{0.06\%}$, and MgO:$Li_{3\%}Ce_{0.06\%}Sm_{0.06\%}$ (listed from left to right, top to bottom): **a.** in the darkness, **b.** under a 12.5 keV electron beam excitation, **c.** after the electron beam is turned off.

PeL spectra were also recorded after excitation of the samples with a 12.5 keV electron beam for 40 s. The measurements were made immediately after switching it off, as the afterglow lasted a relatively short time, approximately one second by eye. The exact PeL decay time cannot be indicated because the duration of PeL was not measured. All PeL spectra are shown in **Figure 8**. These spectra differ from CL spectra in that all emission intensities are many times lower and in that the intensity of the emission bands in the 550−600 nm and 600−650 nm ranges is significantly higher compared to other emission bands. Therefore, the red PeL emission is observed. No correlation was observed between the emission intensities and the dopants concentrations.

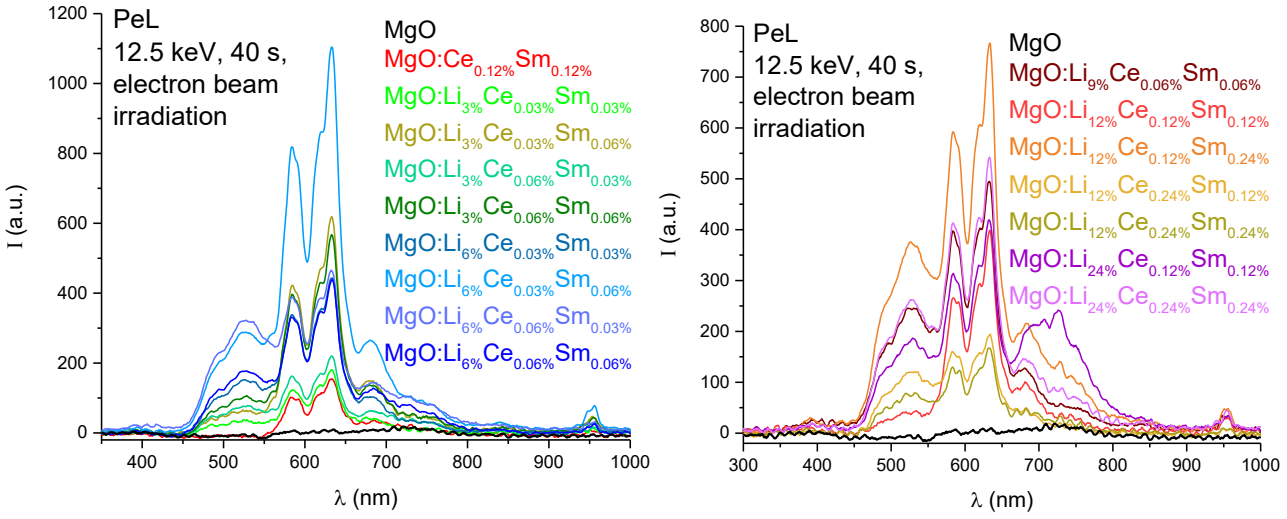

Figure 8. PeL emission spectra after excitation with a 12.5 keV electron beam.

From the obtained PL emission spectra with excitation at 450 nm light (**Figure 5**), it can be noted that the narrow emission peaks at 690, 700, 712, and 721 nm correspond to the emissions of Cr^{3+} ions in oxide host matrix. Identical PL emission spectra with excitation at 450 nm can be observed in the

publication presented by Ristic et al., in which Cr^{3+} ions were doped into Mg_2SiO_4 material.[71] Moreover, according to Guckan et al., chromium is one of the most common impurities in MgO, and it often appears as a broad emission band at about 745 nm in the RL (radioluminescence) emission spectra.[59] The same emission can be observed in the CL spectra of both undoped and doped MgO (**Figure 6**). It is also possible that Cr^{4+} ions produce a broad emission band at 1300 nm in the NIR region.[34] Based on the measured XRF results (**Table S2**), it can be determined that the concentration of chromium in the samples is very low, since the XRF device did not detect it.

In addition, based on the results of studies by Oliveira et al.[60] and Orante-Barron et al.[72], as well as based on the obtained CL spectra (**Figure 6**), it can be concluded that the emission band in the range from 450 nm to 550 nm with maximum at 525 nm and a shoulder at around 490 nm is due to the 5d→4f transition of Ce^{3+}.

Furthermore, it was determined that the narrow emission bands at approximately 948, 1009, and 1090 nm in the NIR region are due to the Sm^{3+} transitions. The NIR emission spectra obtained in this work are similar to the PL emission spectra obtained by Bolton et al. after doping Sm^{3+} into the tellurite glass structure.[73] However, although the emission in the NIR region proves the presence of Sm^{3+} ions in the host material, the emission bands in the visible range of 550−600 nm and 600−650 nm do not correspond to the typical 4f-4f transitions of Sm^{3+} (**Figures 5, 6**). Numerous publications on the topic of Sm^{3+}-doped phosphors report that characteristic 4f-4f emission bands of Sm^{3+} exhibit at approximately 560, 600, and 650 nm.[74–76] Similar results were presented by Kiran et al. in their study, where they synthesized MgO:Sm^{3+} phosphors and investigated their luminescence properties. According to the recorded PL emission spectra under 404 nm excitation, the doped material shows three emission bands at 566, 603, and 651 nm.[65] Slightly different results were obtained by Bishnoi et al.; they also synthesized MgO doped with Sm^{3+} and Li^+ ions. According to their results, phosphors doped with Sm^{3+} and with both Sm^{3+} and Li^+ ions exhibit emission bands at approximately 575, 585, 610, and 628 nm under 405 nm excitation.[61] In addition, Xu et al. demonstrated $Na_2CaSn_2Ge_3O_{12}$:Sm^{3+} phosphors, which show PL emission at around 570, 580, 607, 620, 660, and 670 nm under 255 nm excitation.[77] Based on the results obtained in the above studies, it can be assumed that the emission bands at 577, 590, 611, 625, 655, and 669 shown in the PL spectra (**Figure 5**) also appear due to the 4f-4f transitions of Sm^{3+}. Moreover, it was noted that the collected CL emission spectra (**Figure 6**) coincide with the RL spectra recorded by Oliveira et al., both with doping of Sm^{3+} and with doping of Li^+, Ce^{3+}, and Sm^{3+} ions. This also confirms that the four narrow emissions at 583, 590, 618, and 632 nm are due to the 4f-4f transition of Sm^{3+}. However, for more precise conclusions, further studies and detailed experimental measurements are required.

Based on the obtained results, it was noted that the presence of Li^+ ions in the material improves the luminescence properties of the MgO phosphor, which once again confirms that doping of trivalent ions into a divalent matrix requires the presence of a monovalent ion in the matrix as a charge compensator.

Thus, during the first part of the work, the doped MgO samples were successfully synthesized. Successful doping of Li^+, Ce^{3+}, and Sm^{3+} ions was confirmed by the preservation of the MgO structure and the appearance of characteristic luminescence properties. The obtained samples exhibited good TL properties, demonstrated the ability for OSL, and showed intense emission in both the visible range and the NIR region under 12.5 keV electron beam excitation. In addition, the doped samples show a red PeL emission after electron beam excitation. All these properties of the doped MgO samples demonstrate their potential for NIR optical imaging.

It should also be noted that the MgO:$Li_{12\%}Ce_{0.12\%}Sm_{0.24\%}$ sample was chosen for doping to the glass structure due to its good TL and OSL properties, intense red PeL, and strong CL emission in both the red and NIR regions. In addition, to determine the preservation and efficiency of the luminescence properties of the phosphor after doping into the glass matrix, the optical properties of the fabricated glass-phosphor composites and doped 3D scaffolds were measured and then compared with the results of the MgO:$Li_{12\%}Ce_{0.12\%}Sm_{0.24\%}$ sample.

3.1.1 3D-printed scaffold doped with MgO:$Li_{12\%}Ce_{0.12\%}Sm_{0.24\%}$

Doped 3D scaffolds were printed using a 3D printer and a special ink, which consists of glass powder (30 vol%), MgO:$Li_{12\%}Ce_{0.12\%}Sm_{0.24\%}$ powder (10 wt%), and Pluronic E-127 binder acid (70 vol%). The obtained 3D scaffolds were first heated and then sintered in a furnace. A more detailed process of preparing 3D scaffolds is described in **Table S1** in the supporting information. For the measurement of XRD, TL, and PL, the 3D scaffolds were ground into powder to facilitate the measurement process. Other measurements were conducted using the bulk 3D scaffolds. All measurements were performed using the same parameters, instruments, and settings as for the powder samples.

Figure 9 illustrates the process and result of 3D printing. The second photograph (**b**) shows 3D scaffolds of good quality and shape, while the last one (**d**) shows shapeless 3D scaffolds, which were obtained using ink made with the addition of phosphor. This can be explained by the fact that during 3D printing, the ink was extruded out of a syringe fitted with a nozzle of a certain size, and the relatively large particle size of the added phosphor led to frequent clogging of the nozzle. Therefore, it was decided to extrude the ink directly from the syringe, allowing for the measurement and

comparison of the luminescence properties after sintering. In the future, it is necessary to take into account that the size of phosphor crystals should be as small as possible.

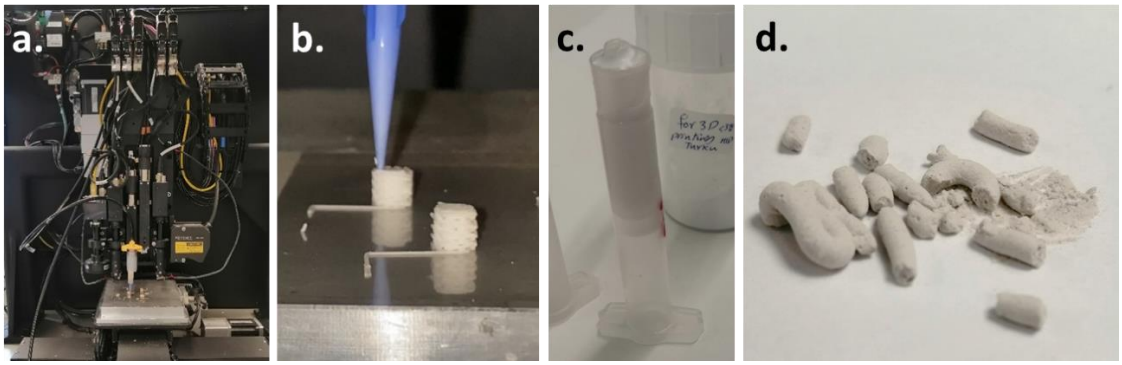

Figure 9. a. 3D printer; **b.** example of good 3D-printed scaffolds; **c.** syringe with ink for 3D printing; **d.** shapeless 3D scaffolds.

The XRD pattern of powdered 3D scaffold (**Figure 10, left**) shows the presence of both crystalline and amorphous phases. The crystalline phase corresponds to the characteristic MgO reflections, while the presence of the amorphous phase is explained by the glass particles. The TL glow curve of the 3D scaffold (**Figure 10, right**) exhibits two TL glow peaks at 190 °C and 298 °C, which also correspond to the TL glow of the MgO:$Li_{12\%}Ce_{0.12\%}Sm_{0.24\%}$ sample. However, the intensity of the TL emission of the 3D scaffold is noticeably weaker because the concentration of phosphor is very low.

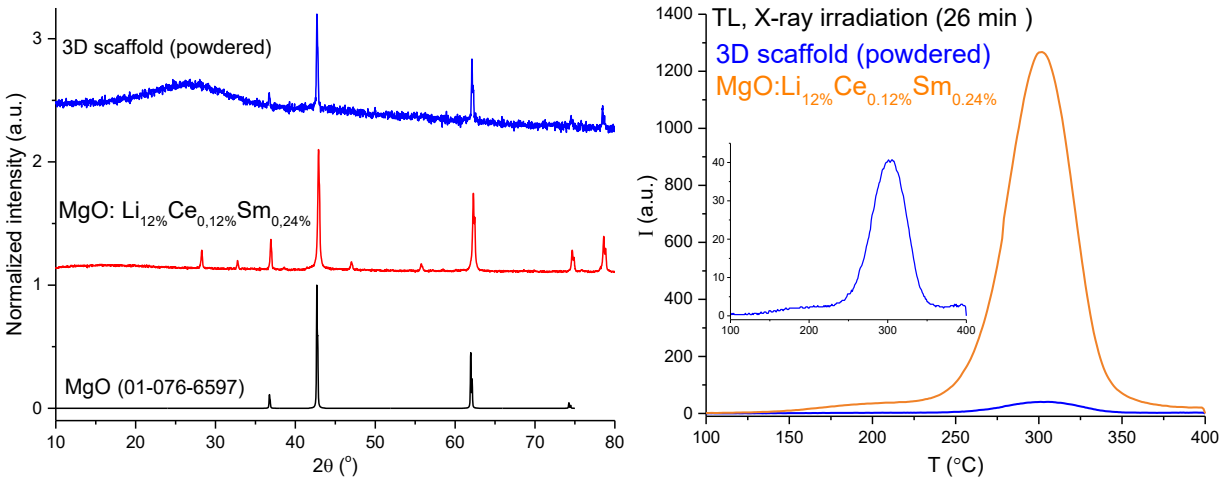

Figure 10. XRD patterns (left) and TL glow curves (right) of MgO:$Li_{12\%}Ce_{0.12\%}Sm_{0.24\%}$ sample and 3D-printed scaffold (powdered).

PL emission spectra of the powdered 3D scaffold (**Figure 11**) were recorded under both 254 nm and 450 nm excitation. It is noticeable that upon excitation with 254 nm light, the PL spectrum exhibits two emission bands with maxima at 585, 610, and 625 nm, which correspond to the emissions of the phosphor. Whereas under 450 nm excitation, the 3D scaffold does not exhibit emission from chromium impurities. However, under both 254 nm and 450 nm excitation, the PL spectra show a

broad emission band in the range from 400 nm to 700 nm, most likely emitting from the glass composite.[78]

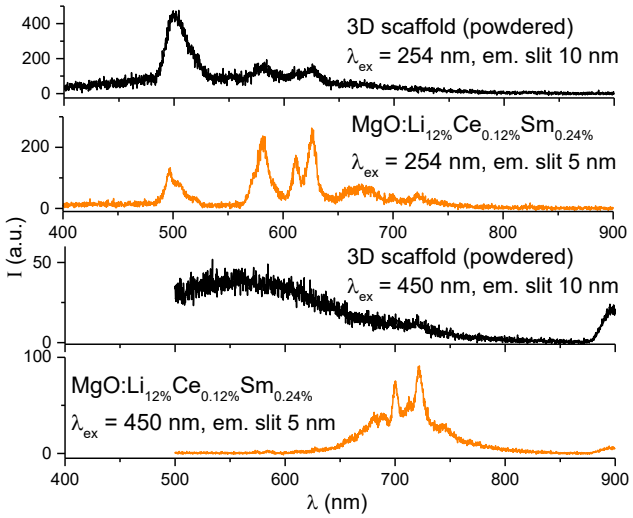

Figure 11. PL emission spectra of MgO:$Li_{12\%}Ce_{0.12\%}Sm_{0.24\%}$ and 3D-printed scaffold (powdered).

CL emission spectra of the bulk 3D scaffolds were recorded and collected in **Figure 12**. It is noticeable that the CL spectrum of the 3D scaffold shows emission similar to that of the powder sample in the visible range, while in the NIR region, the emission disappears, which can also be explained by the low concentration of the phosphor.

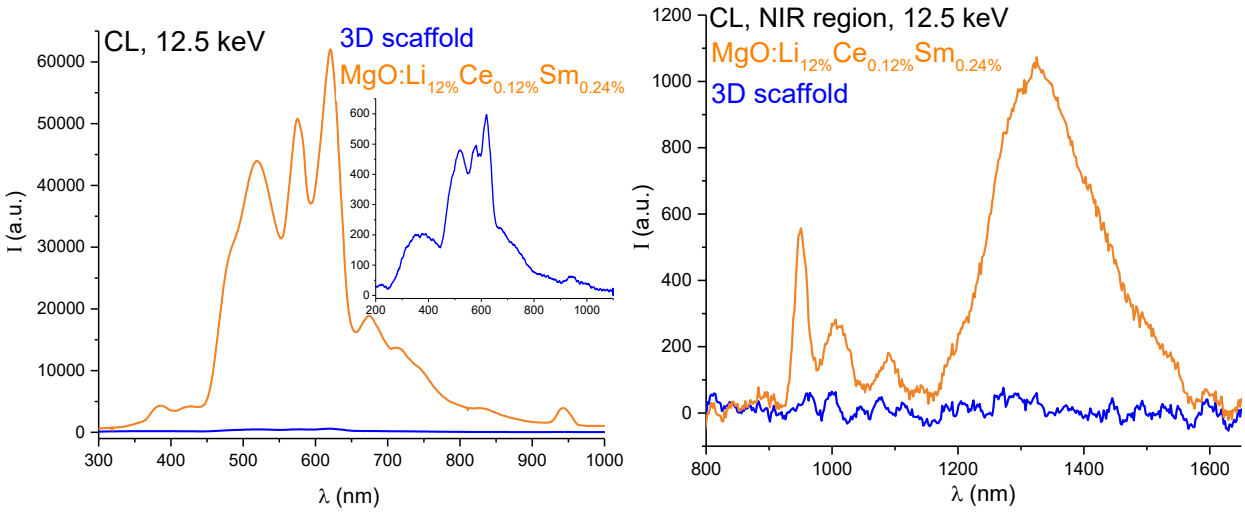

Figure 12. CL emission spectra MgO:$Li_{12\%}Ce_{0.12\%}Sm_{0.24\%}$ and 3D-printed scaffold in both visible (left) and NIR (right) regions.

Furthermore, photographs of 3D scaffolds were taken under different conditions to demonstrate other optical properties. All photographs are collected in **Figure 13**. It can be seen that the second photograph (**b**) shows a 3D scaffold with orange luminescence coming from phosphor particles under a 12.5 keV electron beam. After turning off the electron beam, red PeL emission is also noticeable (**c**). The last two photographs (**d**, **e**) were taken in an attempt to detect OSL properties in doped 3D

scaffolds in the same way as in doped MgO samples. In both photos, 3D scaffolds were stimulated with a 980 nm laser (without (**d**) and after (**e**) X-ray irradiation). It is interesting that in both cases, a bright green luminescence is noticeable, which indicates the absence of OSL properties, but shows the appearance of upconversion luminescence in the doped 3D scaffold. The origin of the upconversion was not studied further.

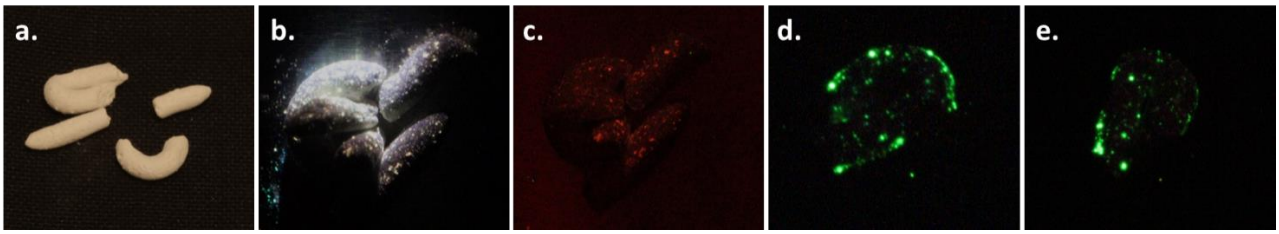

Figure 13. 3D scaffolds doped with MgO:$Li_{12\%}Ce_{0.12\%}Sm_{0.24\%}$ powder: **a.** under room lighting, **b.** under electron beam excitation, **c.** PeL after electron beam excitation, **d.** under 980 nm laser stimulation (without X-ray pre-irradiation), **e.** under 980 nm laser stimulation, after X-ray irradiation (OSL).

Thus, it can be concluded that the luminescence properties of the phosphor are preserved after sintering with glass particles, except for the OSL properties.

3.1.2 Glass-phosphor composites doped with MgO:$Li_{12\%}Ce_{0.12\%}Sm_{0.24\%}$

The same MgO:$Li_{12\%}Ce_{0.12\%}Sm_{0.24\%}$ sample was doped into the phosphate glass by three different methods described in **Table S1**. The names of the doped glass samples correspond to their fabrication methods, namely Remelt, DDM, and Sandwich. The PL and CL spectra were measured for all the fabricated glass-phosphor composites.

It is interesting that the PL emission spectra of Remelt and DDM glass-phosphor composites under 361 nm excitation demonstrate three emission bands at 560, 600, and 650 nm (**Figure 14**), which correspond to typical 4f-4f transitions of Sm^{3+} ions, in contrast to the PL emission of doped phosphor.[65] This may indicate that doping of phosphor into the glass matrix has a positive effect on the luminescence properties of doped MgO and somehow affects the luminescence centres of Sm^{3+} ions. Further research is needed to make more accurate conclusions. However, the PL emission from Sm^{3+} of the Sandwich glass sample coincides with the emission of the phosphor under 254 nm excitation, which can be explained by the fact that the phosphor is located between two glass layers and is not directly doped into the glass matrix. Also, this glass sample exhibits a broad emission band in the range from 400 nm to 700 nm, probably emitted from the glass matrix under 254 nm excitation.[78]

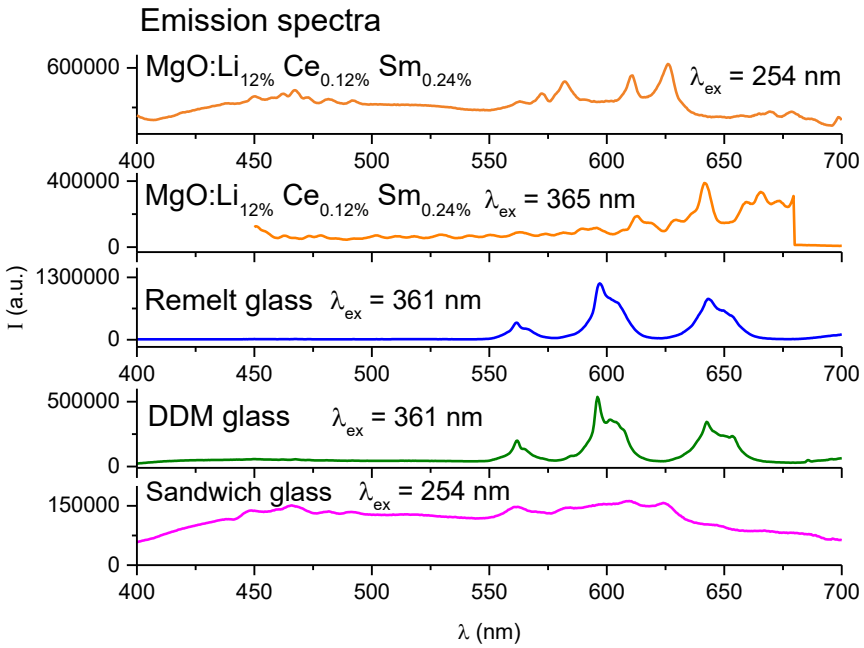

Figure 14. PL emission spectra of MgO:$Li_{12\%}Ce_{0.12\%}Sm_{0.24\%}$ powder and glass-phosphor composites.

Figure 15 contains photographs visually illustrating other optical properties of the glass-phosphor composites. The photographs in the first column demonstrate doped glass samples under room lighting, while the second column shows samples under a 12.5 keV electron beam excitation. It is noticeable that the glasses have an orange-red emission. The third column shows that after switching off the electron beam, the glass samples demonstrate red PeL emission, which lasts visually longer than that of phosphors. It is also noticeable that Remelt glass demonstrates uniform glow, while the other two glass samples show emission only where the phosphor is concentrated the most. The experiment to identify OSL properties in glass samples was also repeated. The photographs in the fourth column show glasses that were pre-irradiated with X-rays and stimulated with a 980 nm laser during photography. No glow is visible, so it can be said that OSL properties also disappear after doping the phosphor into the glass matrix.

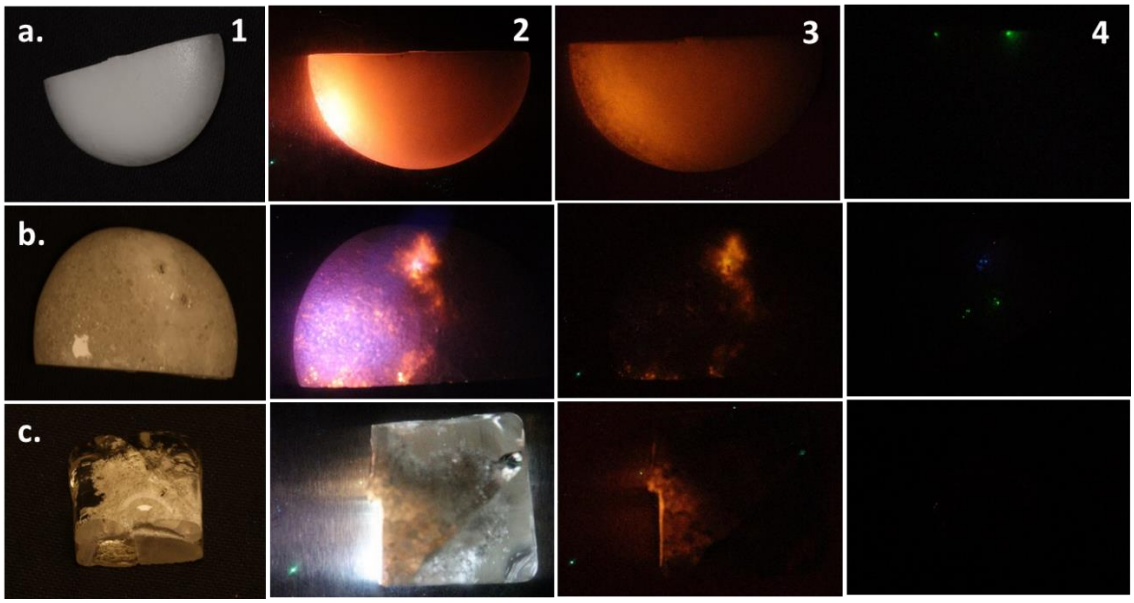

Figure 15. Row a: Remelt glass; row b: DDM glass; row c: Sandwich glass. Column 1: under room lighting; column 2: under electron beam excitation; column 3: PeL after electron beam excitation; column 4: OSL experiment (under 980 nm laser stimulation, after X-ray irradiation).

In addition, the CL emission spectra of doped and undoped (reference) glass samples were recorded under excitation of a 12.5 keV electron beam. All collected spectra are shown in **Figure 16**. In the emission spectra of the Remelt and DDM glass samples, three emission bands are noticeable at 600, 650, and 700 nm, probably corresponding to transitions of Sm^{3+} ions.[65] The emission intensity in the range of 450−550 nm significantly decreased, and a new emission band in the range from 300 nm to 450 nm appeared. It is noticeable that there is a weak emission in the same range in the CL spectrum of the reference glass, which may indicate that the new emission comes from the glass matrix, but there is also a possibility that it is due to Ce^{3+} ions.[79] In the NIR region, CL emission at 950 nm exhibits only in the Remelt glass sample. Sandwich glass shows emission similar to that of $MgO:Li_{12\%}Ce_{0.12\%}Sm_{0.24\%}$ because the phosphor has not been directly doped into the glass matrix.

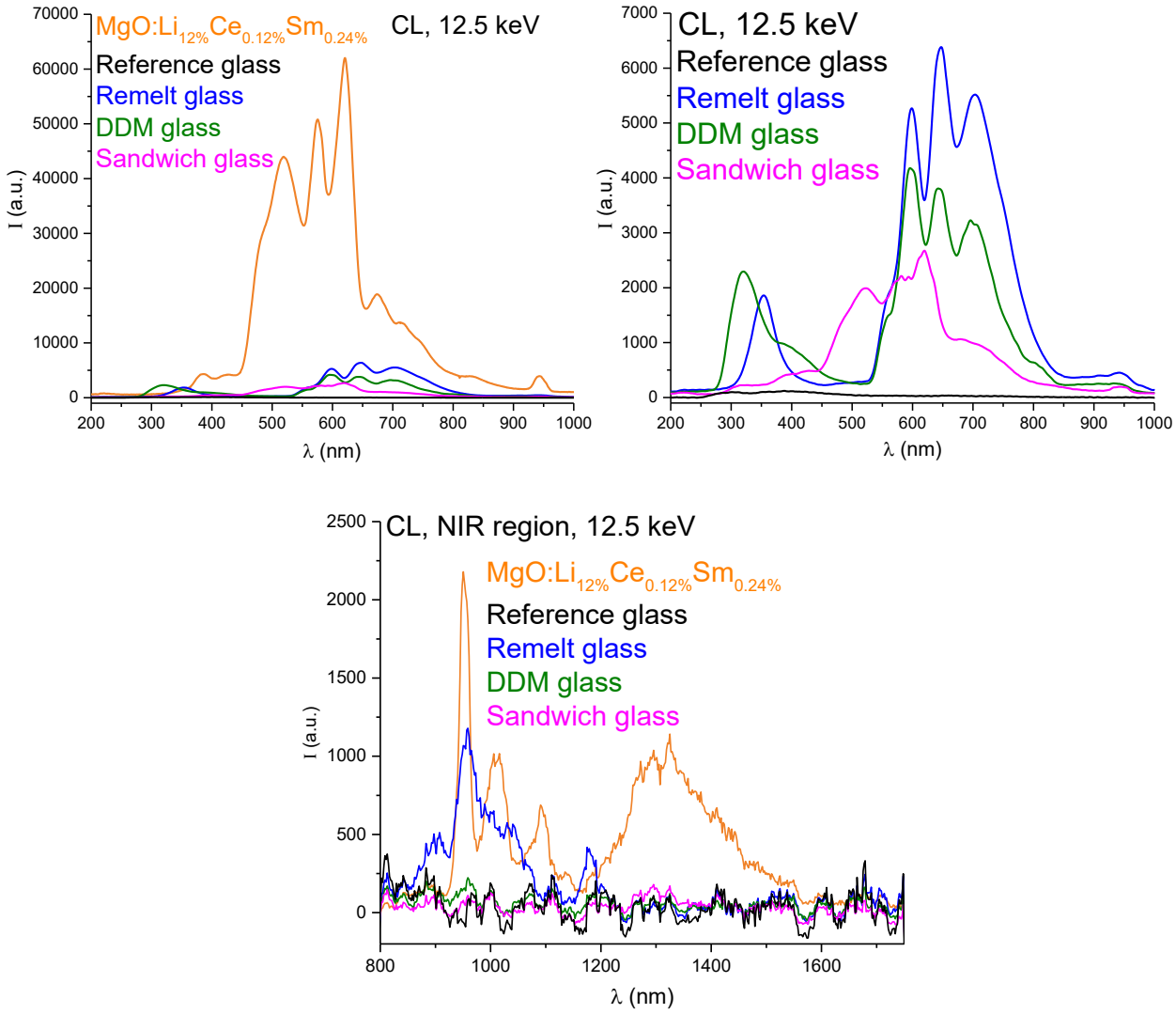

Figure 16. CL emission spectra of $MgO:Li_{12\%}Ce_{0.12\%}Sm_{0.24\%}$ powder and glass-phosphor composites in both visible and NIR regions.

Thus, it can be concluded that the fabricated glass-phosphor composites preserve and to some extent improve the luminescence properties of the doped phosphor. According to the collected CL spectra, it is evident that the luminescence intensity is noticeably weaker, but this is explained by the low concentration of phosphor in the glass matrix (2.5−5 wt%). It is also possible that with higher-energy excitation, the emission intensity will become much stronger.

3.2 $Mg_{14}Ge_5O_{24}$ (MGO) phosphor

During this part of the work, seven batches of MGO samples doped with different dopants (Cr^{3+}, Mn^{4+}, Ho^{3+}, Yb^{3+}, Nd^{3+}, Tm^{3+}) were synthesized. The batches with co-doping of Cr^{3+} and Ln^{3+} (Ho, Tm, Nd) ions did not show any significant results; therefore, they will not be included in this work. Whereas doping of Mn^{4+}, $Cr^{3+,}$ and Yb^{3+} improved and modified the luminescence properties of the phosphor. However, at the time of fabrication of glass composites and 3D scaffolds, only two batches of MGO samples doped with Cr^{3+} and co-doped with Cr^{3+} and Mn^{4+} were synthesized. Therefore, the

best sample from each batch was selected for doping into the glass matrix. In this part of the work, the obtained results of samples from the first two batches are described; however, the most important CL emission spectra of samples from other batches were collected in **Figure S2** in the supporting information.

As with the first material, undoped MGO was first synthesized as a reference sample. To confirm the success of synthesizing the desired material, the XRD pattern of the undoped sample was measured and subsequently compared with the reference XRD patterns from the ICDD PDF-4+ reference database. Both diffractograms are shown in **Figure 17**, and since they are identical, it can be concluded that the synthesis was successful. The $Mg_{14}Ge_5O_{24}$ reference diffractogram number is 04-010-1371.

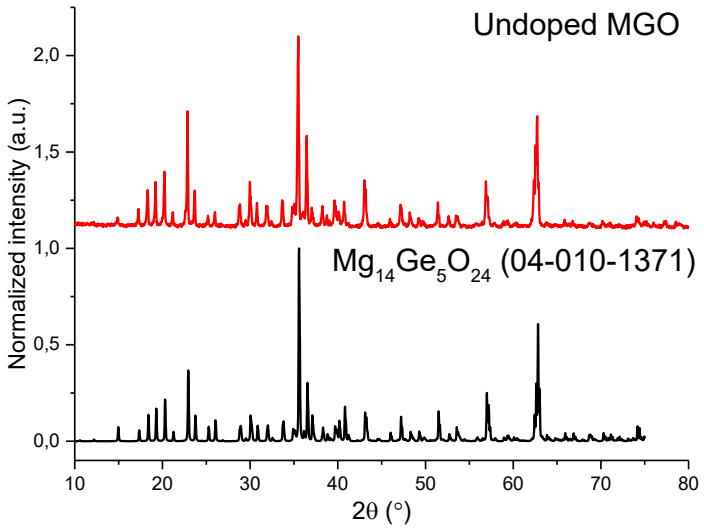

Figure 17. XRD patterns of $Mg_{14}Ge_5O_{24}$.

3.2.1 MGO:$Cr_{x\%}$ batch

MGO samples of the first batch were doped with different concentrations of Cr^{3+} ions from 1% to 19%. The diffractograms shown in **Figure 18** were measured for all synthesized samples. The presence of only one main phase was detected, which may indicate successful doping of the Cr^{3+} into the host matrix.

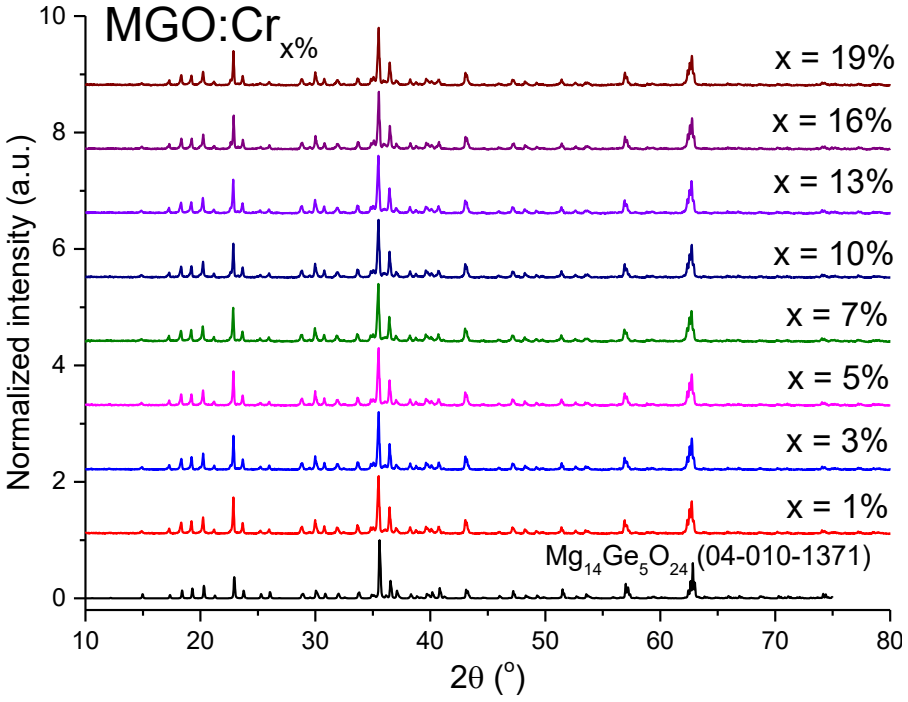

Figure 18. XRD patterns of MGO doped with different concentrations of Cr^{3+}.

In addition, the PL emission spectra were recorded for all samples excited by 302, 420, 670, and 730 nm light (**Figures 19-21**). The undoped sample exhibits emission in the range from 600 nm to 700 nm, centered at 630 and 660 nm, under 302 and 420 nm excitation. According to Xue et al., emission in this range occurs due to d-d transitions of Mn^{4+} ions in the MGO host phosphor.[80] Weak emission in the NIR region is also observed under 420 and 730 nm excitation, which may indicate the presence of chromium impurities in the host matrix.[67] According to the XRF measurement results from **Table S3**, it can be seen that undoped MGO contains a small amount of both manganese and chromium impurities, which can directly affect the luminescence properties of the undoped host material.

The PL spectra of the doped samples also show intense red emission in the range from 600 nm to 700 nm under 302 and 420 nm excitation (**Figures 19a and 20**). This may also indicate the presence of manganese impurities, which is confirmed by the XRF results from **Table S3**. It can be noted that with an increase in the concentration of Cr^{3+} ions in the host matrix, this emission is gradually quenched. The same trend can be seen in the photograph of the doped samples, which exhibit red emission under 302 nm UV lamp excitation (**Figure 19c**). In addition, under excitation at 420 nm, the doped samples exhibit two emission bands of 700−1000 nm and 1100−1600 nm in the NIR region (**Figure 20**). According to Wang et al., the first emission is due to the d-d transitions of Cr^{3+} ions, while the presence of the second emission indicates the formation of Cr^{4+} ions during the synthesis.[67] From the PL spectra, it is noticeable that with an increase in the concentration of Cr ions, the intensity of both NIR emissions increases.

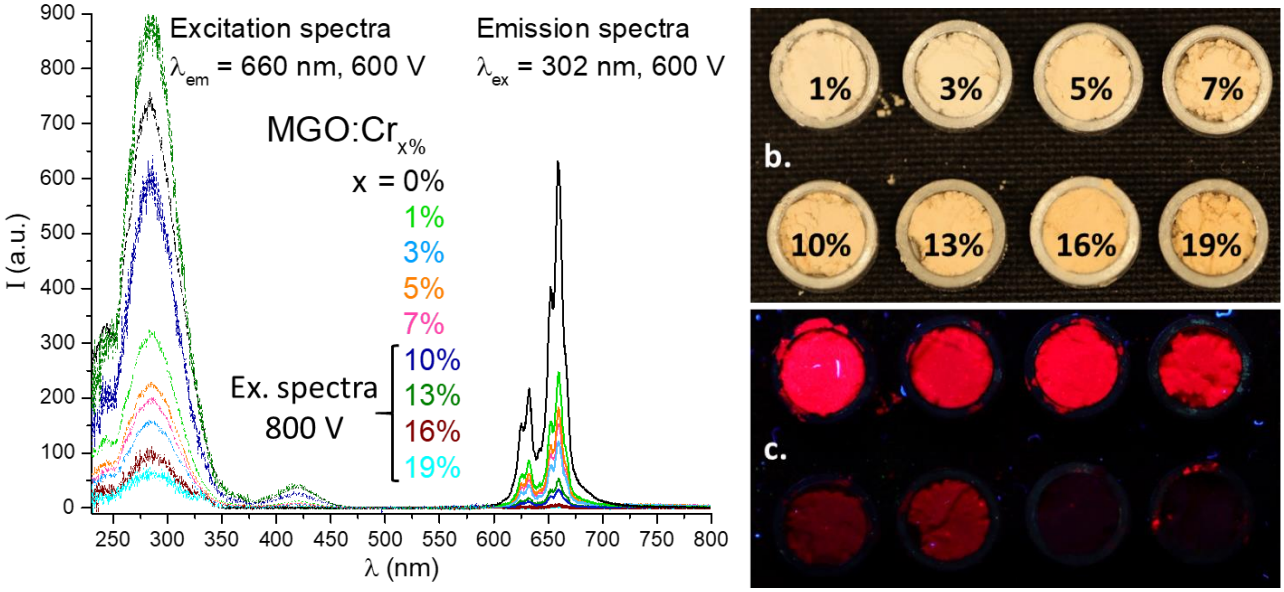

Figure 19. PL (λ_{ex} = 302 nm) and PLE (λ_{em} = 660 nm) spectra of MGO doped with different concentrations of Cr^{3+} (**a**). Photographs of samples under room lighting (**b**) and under UV lamp (302 nm) excitation (**c**).

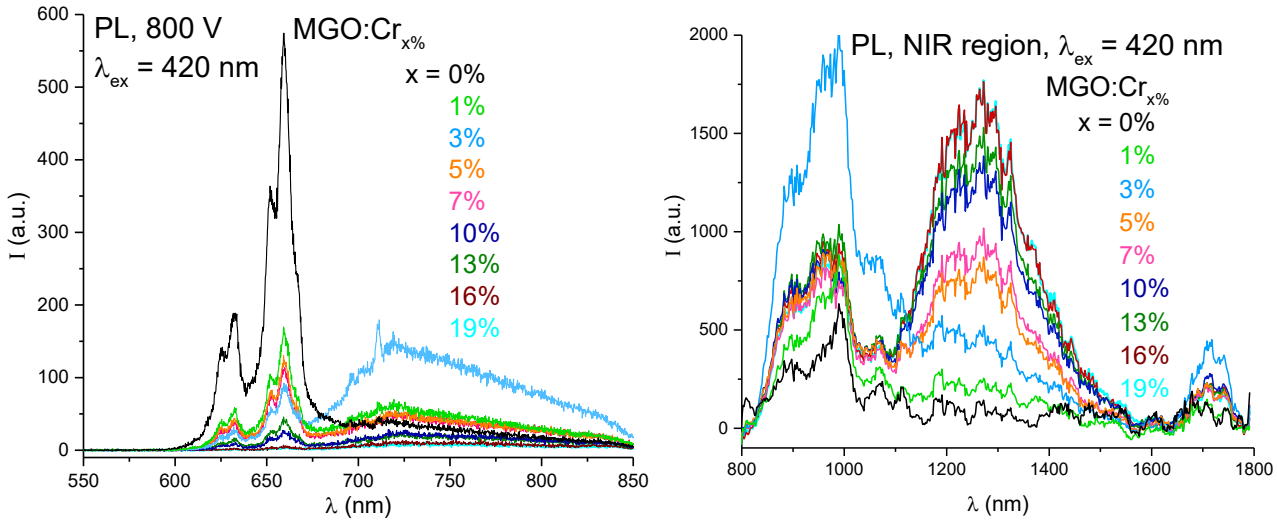

Figure 20. PL emission spectra in both the visible range (left) and the NIR region (right) under 420 nm excitation.

It is significant for this work that the samples demonstrate emissions in the NIR-II region under 670 and 730 nm excitation (**Figure 21**), since this material can be used as a phosphor for the fluorescence NIR imaging. An increase in the emission intensity at 1300 nm can also be observed with increasing concentration of chromium ions in the host matrix.

The quenching of Mn^{4+} emission in the range from 600 to 700 nm could be explained by the fact that Mn^{4+}, along with both $Cr^{3+/4+}$ ions, tends to replace Ge^{4+} ions in the host matrix[34]; therefore, with an increase in the concentration of Cr ions, more of their luminescence centers are formed. At the same time, Mn^{4+} will have fewer free Ge^{4+} vacancies.

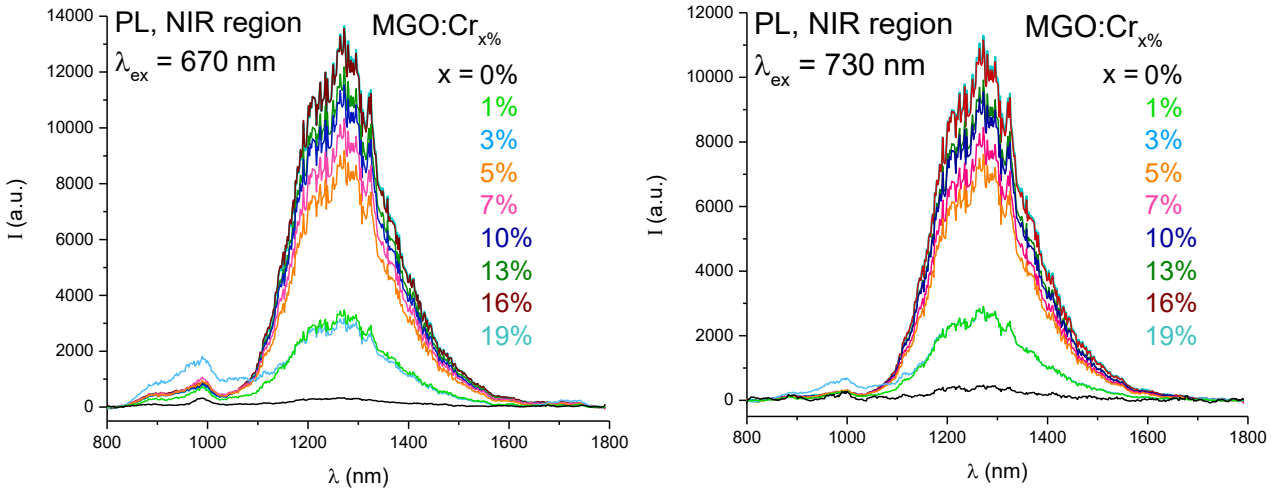

Figure 21. NIR PL emission spectra under 670 nm (left) and 730 nm (right) excitation.

Additionally, CL emission spectra were recorded under 12.5 keV electron beam, but for some samples with very intense emission, the electron beam power was reduced (**Figure 22**). The CL spectra show a broad band of intense emission in the range from 600 to 1100 nm with maxima at 750 and 910 nm, as well as weak emission at 1250 nm for samples with a Cr concentration of ≥ 5%. According to Zeng et al., the broad band of RL emission in the range from 650 to 1200 nm also corresponds to transitions of Cr^{3+} ions.[81] The most intense emission is observed for the MGO:$Cr_{1\%}$ and MGO:$Cr_{3\%}$ samples, while for the MGO:$Cr_{x\%}$ (x ≥ 5%) samples, the emission in the NIR-I region is gradually quenched, which can be explained by concentration quenching. The most intense emission in the NIR-II region is observed for the MGO:$Cr_{7\%}$ and MGO:$Cr_{10\%}$ samples.

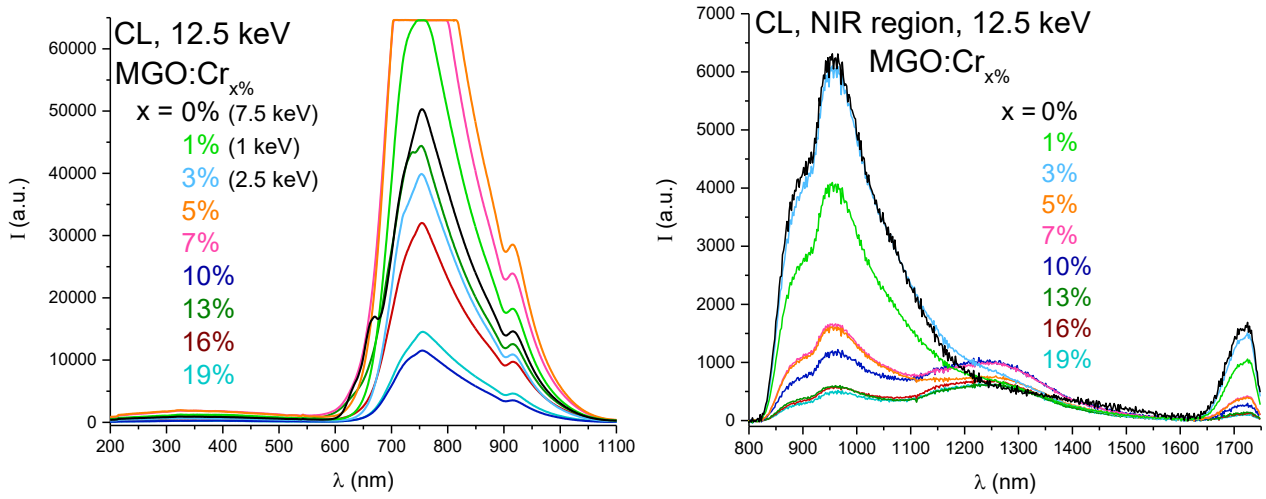

Figure 22. CL emission spectra in both the visible range (left) and the NIR region (right) under electron beam excitation.

Thus, based on the obtained results, it can be conclude that Cr-doped MGO is a promising candidate as a phosphor for both fluorescence and X-ray excited NIR imaging. For doping into the glass matrix,

the MGO:$Cr_{19\%}$ sample was chosen because it showed the most intense emission in the NIR-II region under NIR light excitation. Whereas, for co-doping with Mn^{4+} ions, the MGO:$Cr_{10\%}$ sample was selected because it showed the weakest emission in the NIR-I region under electron beam excitation.

3.2.2 MGO:$Cr_{10\%}Mn_{x\%}$ batch

In an attempt to improve the luminescence properties in the NIR region, MGO:$Cr_{10\%}$ phosphor was doped with Mn^{4+} ions with different concentrations from 0.5% to 2%. The XRD patterns were measured for all synthesized samples (**Figure 23**); they also showed the presence of only the MGO phase.

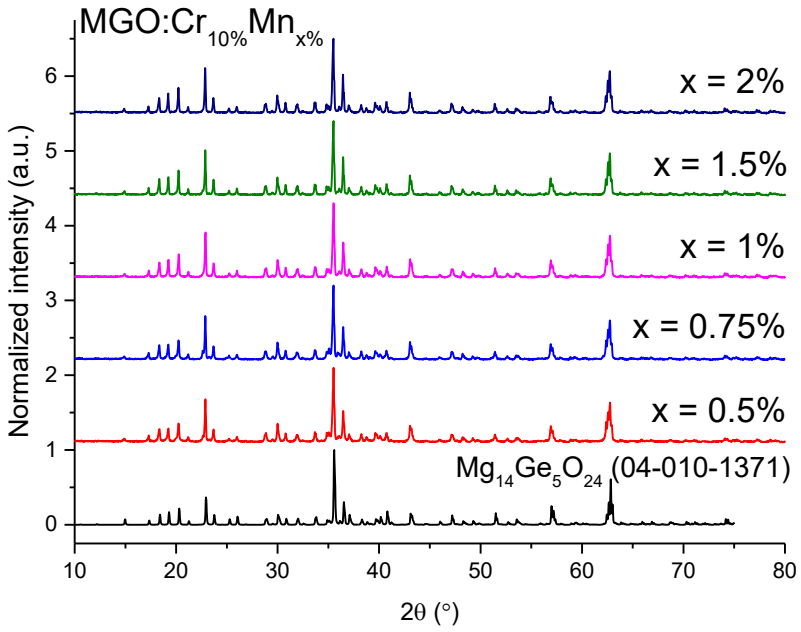

Figure 23. XRD patterns of MGO:$Cr_{10\%}$ samples doped with different amounts of Mn^{4+} ions.

The PL emission spectra of all samples were recorded under 302, 420, 670, and 730 nm excitation (**Figures 24-26**). The samples of the second batch also exhibit three emission bands in the ranges of 600-700 nm, 700-1000 nm, and 1100-1600 nm.

It is noticeable that under 302 nm excitation, the samples have a bright red emission, the intensity of which increases with increasing concentration of Mn^{4+} ions in the phosphor (**Figure 24**). The same tendency is observed for the samples under 420 nm excitation (**Figure 25**). Emission at 660 nm refers to d-d transitions of Mn^{4+} ions, as was already mentioned above. Therefore, an increase in its intensity with increasing concentration (up to an acceptable limit) is logical. In addition, it is noticeable that under 420 nm excitation, the emission intensity in the range of 700−1100 nm also increases with increasing Mn^{4+} concentration. However, in the NIR-II region, in contrast, it weakens for samples with a Mn concentration of ≥ 1%.

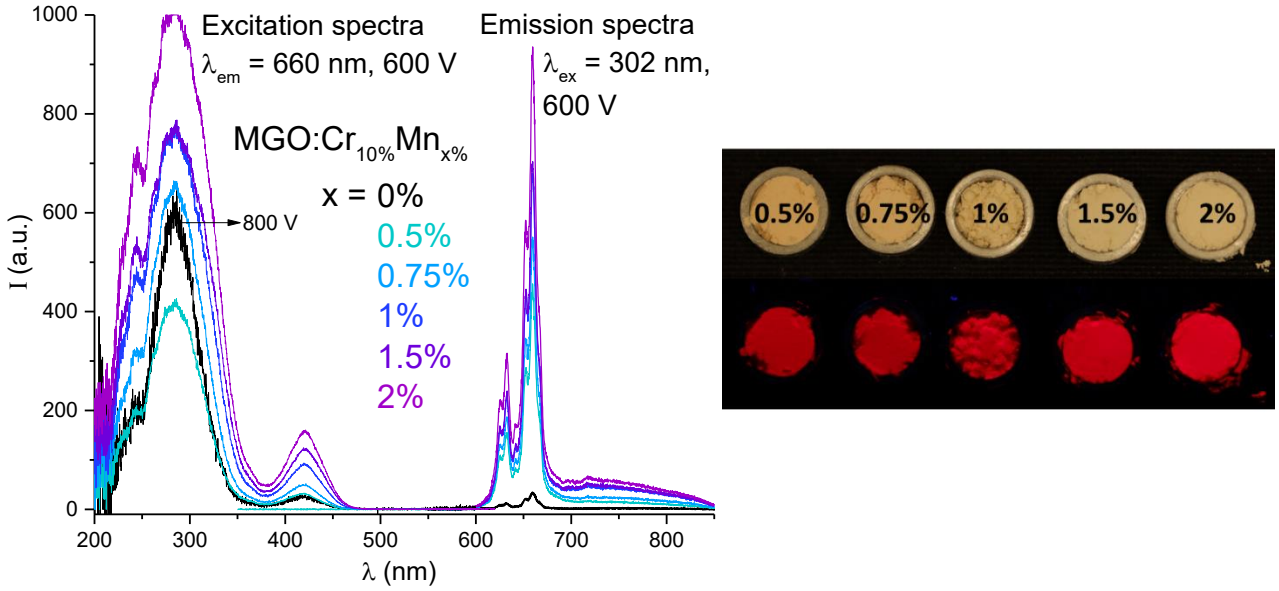

Figure 24. PL (λ_{ex} = 302 nm) and PLE (λ_{em} = 660 nm) spectra of MGO:$Cr_{10\%}$ samples doped with different amounts of Mn^{4+} ions (left). Photographs of samples under room lighting and 302 nm UV lamp excitation

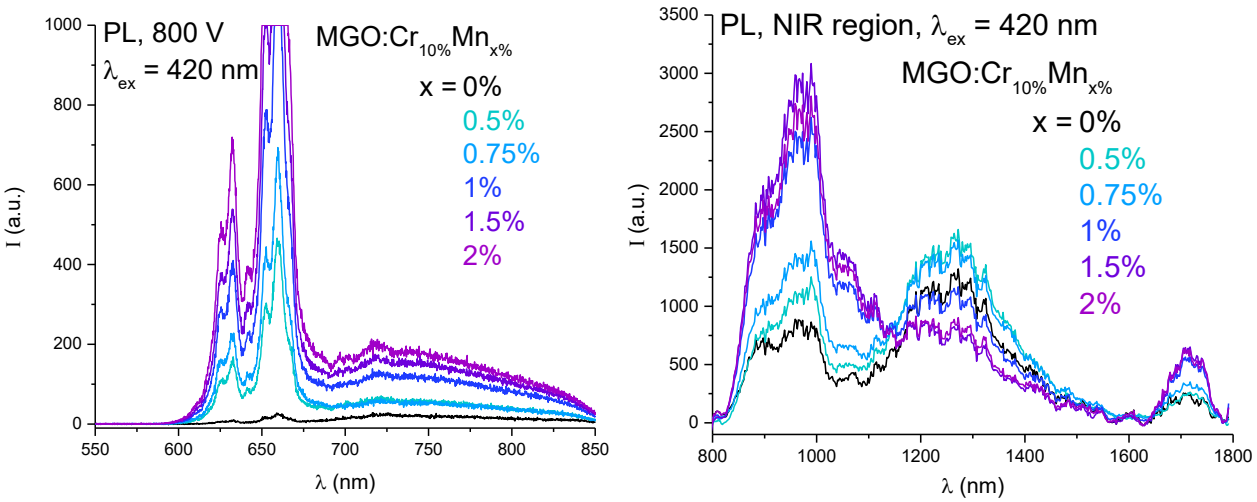

Figure 25. PL emission spectra in both the visible range (left) and the NIR region (right) under 420 nm excitation.

The PL emission spectra (**Figure 26**) of the samples excited by NIR light show weakening of the emission intensity with increasing Mn^{4+} concentration. The same trend can be noticed in the CL emission spectra shown in **Figure 27**. With an increasing concentration of Mn^{4+} ions, the emission in the NIR-I region increases while in the NIR-II region it decreases.

Thus, it can be assumed that the emission increase in the range from 700 to 1000 nm with an increase in the concentration of Mn^{4+} ions in the host matrix may be associated with the energy transfer from the Mn^{4+} to Cr^{3+},[82] or the presence of Mn^{4+} in the matrix can somehow facilitate the formation of active luminescence centers of Cr^{3+}. While the weakening of the emission in the NIR-II region may be because the presence of another tetravalent ion in the host matrix can limit the formation of Cr^{4+}

ions during synthesis, thereby reducing their concentration, at the same time more Cr^{3+} ions are formed, which can also be the reason for the increase in the emission intensity in the NIR-I region.

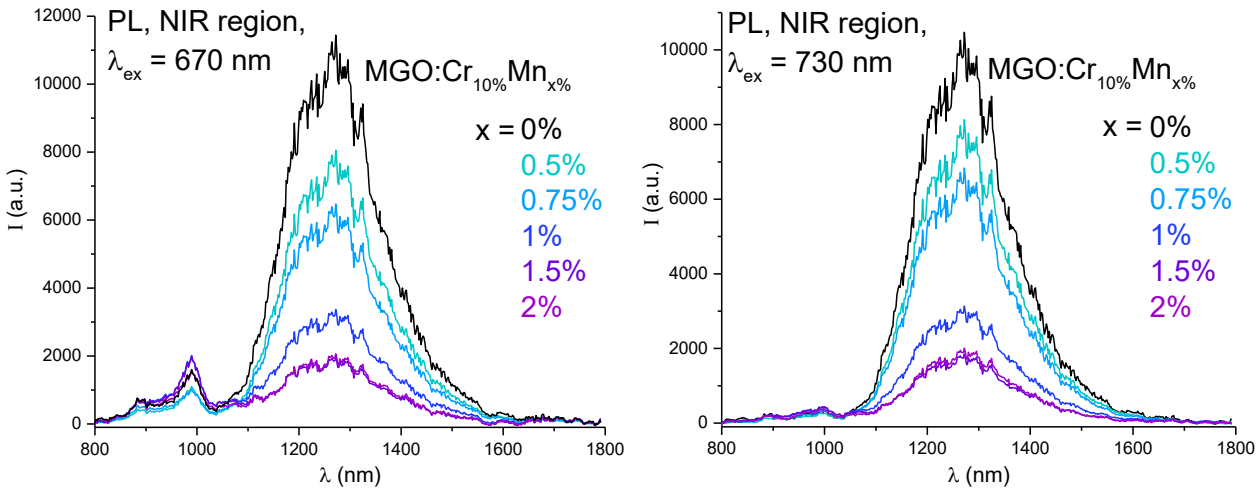

Figure 26. NIR PL emission spectra under 670 nm (left) and 730 nm (right) excitation.

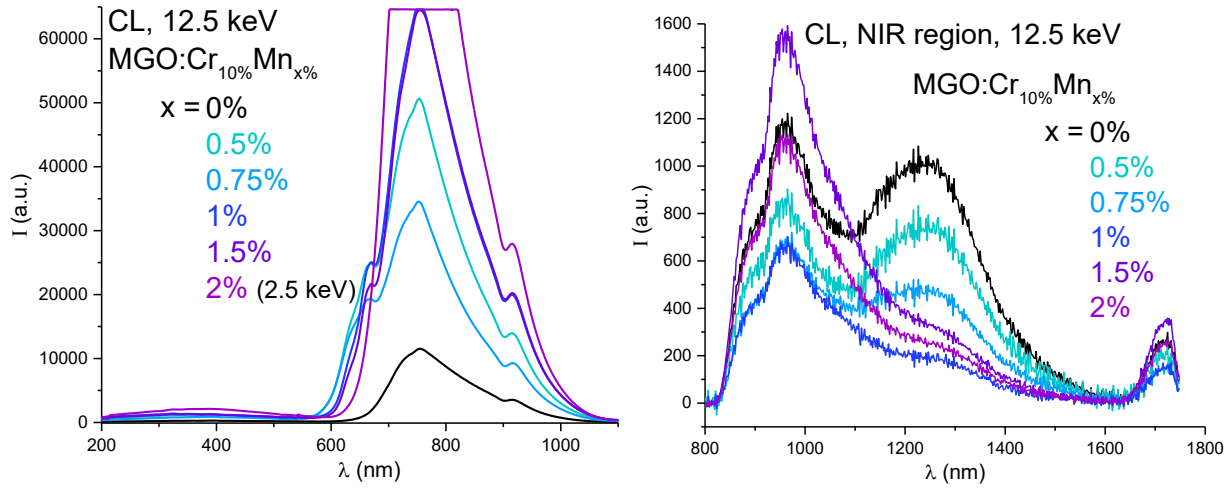

Figure 27. CL emission spectra in both the visible range (left) and the NIR region (right) under electron beam excitation.

Based on the obtained results, it can be concluded that Mn^{4+} improves the luminescence properties of MGO:$Cr_{10\%}$ phosphor, but only in the NIR-I region. The samples of this batch with high concentrations of Mn^{4+} ions could be used as phosphors for X-ray excited NIR imaging because they show intense emission in the NIR-I region under electron beam excitation. However, the sample with the lowest Mn^{4+} concentration was chosen for doping into the 3D scaffold since it showed relatively intense emission in both NIR-I and NIR-II regions.

3.2.3 3D-printed scaffolds doped with MGO phosphors

For doping into the 3D scaffold's structure, the two best samples from the first two batches were selected: MGO:$Cr_{19\%}$ and MGO:$Cr_{10\%}Mn_{0.5\%}$. As in the case of the previous material, **Figure 28**

contains photographs demonstrating the 3D printing ink (**a**), the 3D printing process (**b**), and the printed doped 3D scaffolds (**c, d**). It can be seen that the shape of the printed 3D scaffolds is also far from ideal, indicating that the crystal sizes of both phosphors were too large for the used nozzle. However, a couple of 3D scaffold samples doped with MGO:$Cr_{10\%}Mn_{0.5\%}$ were successfully printed using proper print settings for the prepared ink (**c**).

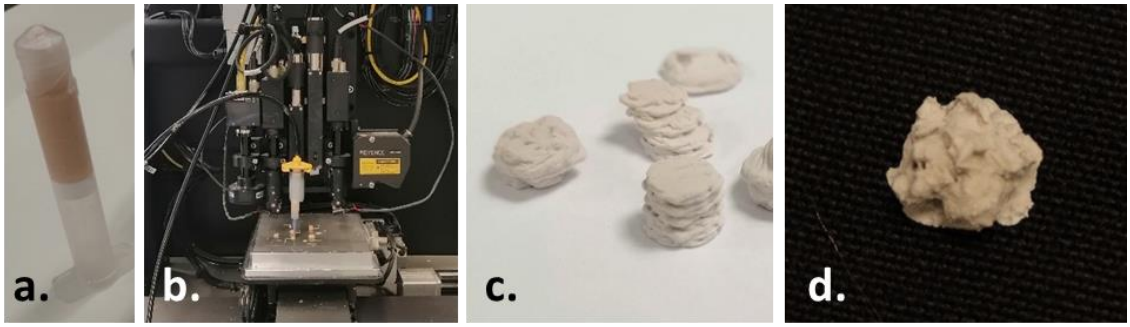

Figure 28. a. Syringe with the ink for 3D printing; **b.** 3D printer; **c.** 3D scaffolds doped with MGO:$Cr_{10\%}Mn_{0.5\%}$; **d**. 3D scaffold doped with MGO:$Cr_{19\%}$.

To measure the XRD patterns and PL properties of the doped 3D scaffolds, they were ground into powder. In the measured diffractograms (**Figure 29**), two phases are visible: amorphous and crystalline. The most intense reflections of the crystalline phase coincide with those of the MGO phase, while the presence of the amorphous phase confirms the presence of glass in the 3D scaffolds.

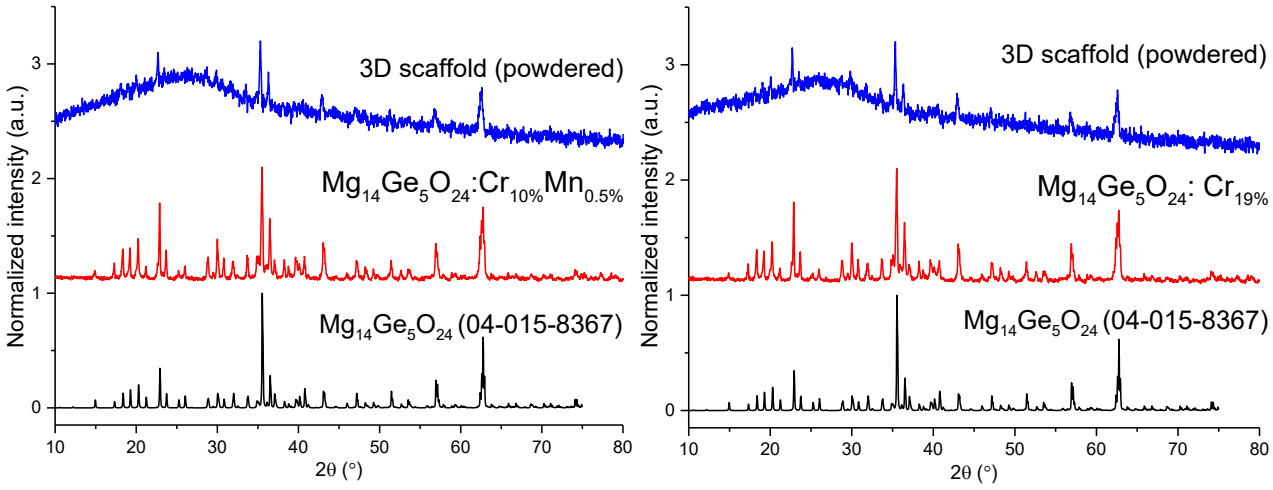

Figure 29. XRD patterns of 3D scaffolds doped with MGO:$Cr_{10\%}Mn_{0.5\%}$ sample (left) and with MGO:$Cr_{19\%}$ sample (right).

In addition, the PL emission spectra of the powdered 3D scaffolds were recorded and are collected in **Figures 30** and **31**. The PL spectra of the 3D scaffold doped with MGO:$Cr_{10\%}Mn_{0.5\%}$ exhibit weak emission in the range from 620 nm to 670 nm, excited by 302 nm light. The emission in this range corresponds to the emission of the phosphor itself. It is also noticeable that under 302 and 420 nm

excitation, the emission in the NIR-I region (700−1000 nm) is preserved. Whereas, under NIR light excitation, the emission intensity in the range of 1100−1600 nm noticeably weakens. The weakening of the emission can be explained by the fact that the concentration of the phosphor in the 3D scaffold is very low (10 wt%).

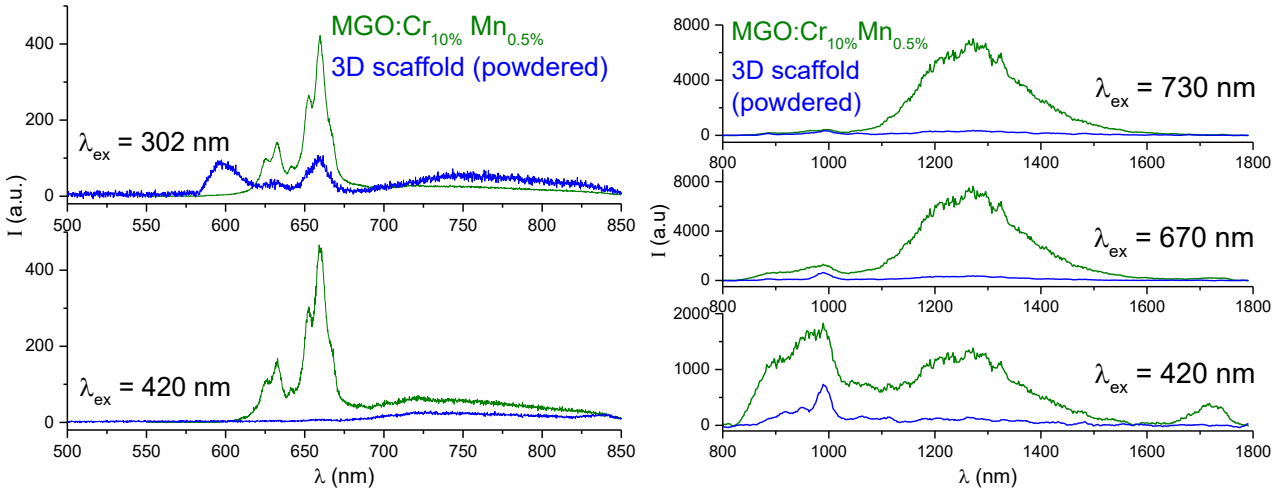

Figure 30. PL emission spectra of MGO:$Cr_{10\%}Mn_{0.5\%}$ and powdered 3D scaffold doped with MGO:$Cr_{10\%}Mn_{0.5\%}$.

The PL spectra of 3D scaffold doped with MGO:$Cr_{19\%}$ show emission that is completely consistent with the emission of the phosphor under UV excitation. NIR light-excited emission in the NIR-II region is also present, but it is noticeably weaker.

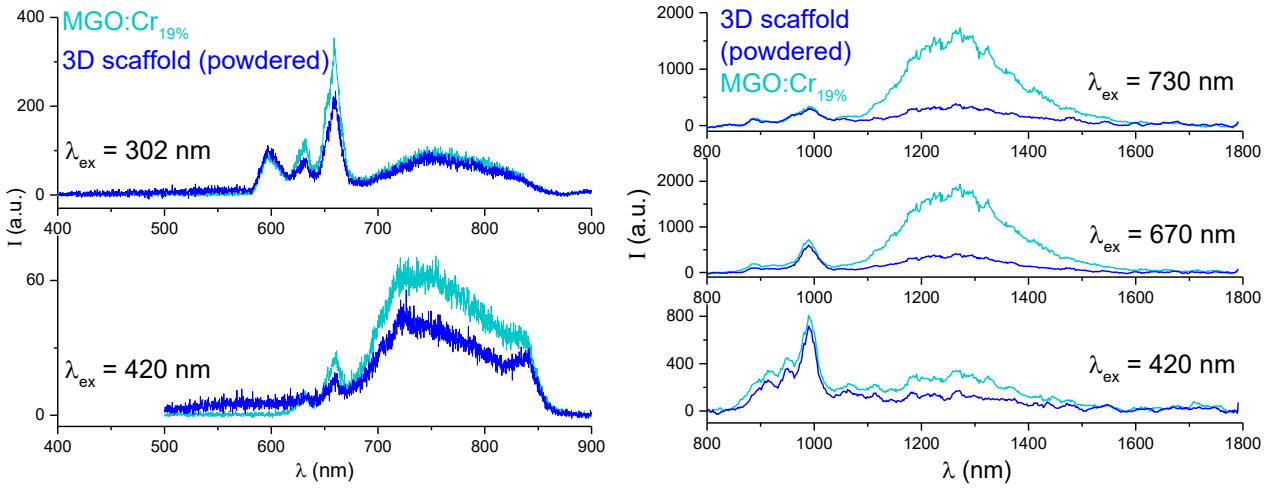

Figure 31. PL emission spectra of MGO:$Cr_{19\%}$ and powdered 3D scaffold doped with MGO:$Cr_{19\%}$.

Figure 32 shows photographs of doped 3D scaffolds under room lighting (**a, c**) and under electron beam excitation (**b, d**). The 3D scaffolds under 12.5 keV electron beam excitation exhibit a violet glow, which is attributed to the camera's perception and recording of NIR emission. In addition, the recorded CL emission spectra of both bulk 3D scaffolds are shown in **Figures 33** and **34**. It can be

seen that they coincide with the CL spectra of phosphors, but the exhibited emission is noticeably weaker.

Thus, based on the obtained results, it can be concluded that the luminescence properties of the phosphors were preserved after sintering with glass powder. Good results were demonstrated by 3D scaffolds doped with MGO:$Cr_{19\%}$ phosphor.

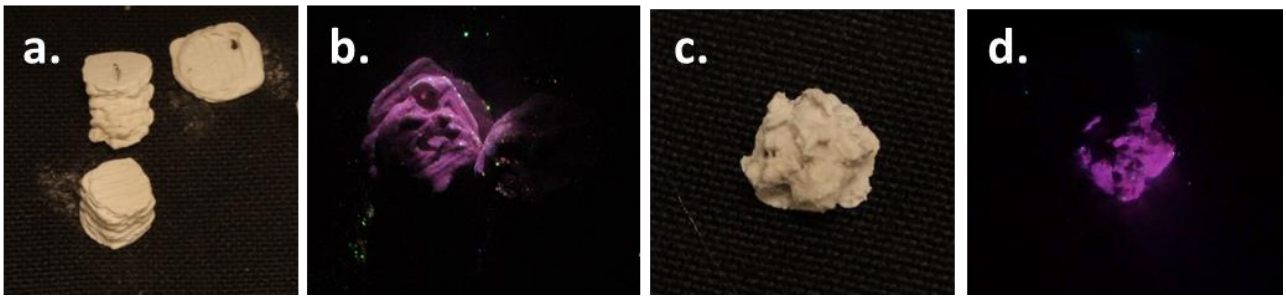

Figure 32. 3D scaffolds doped with MGO:$Cr_{10\%}Mn_{0.5\%}$ (**a, b**): **a.** under room lighting, **b**. under electron beam excitation; 3D scaffold doped with MGO:$Cr_{19\%}$ (**c, d**): **c.** under room lighting, **d**. under electron beam excitation.

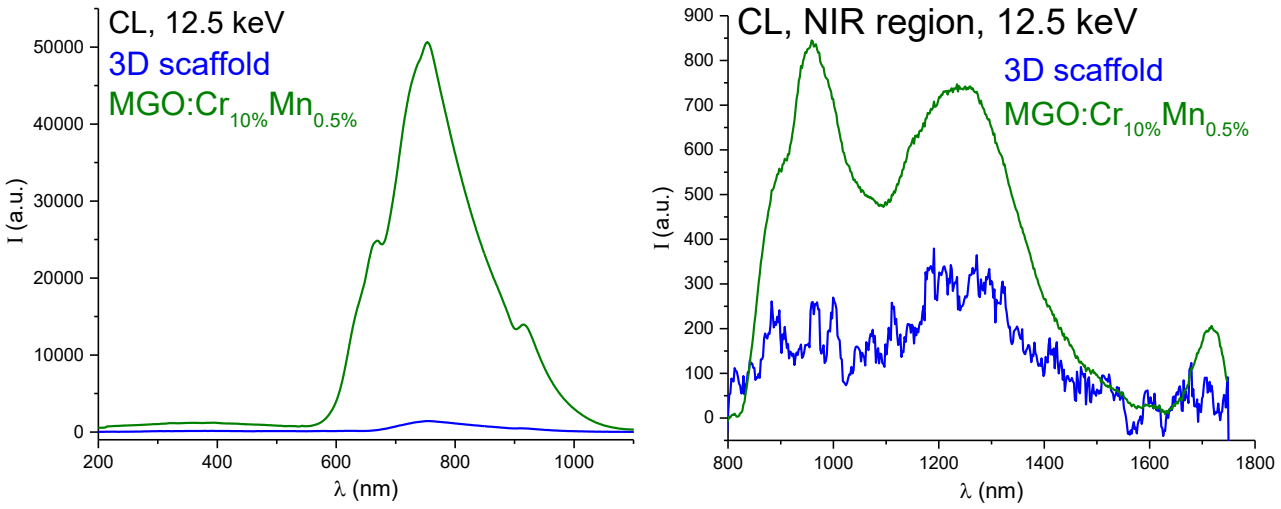

Figure 33. CL emission spectra of 3D scaffold doped with MGO:$Cr_{10\%}Mn_{0.5\%}$ in both the visible range (left) and the NIR region (right) under electron beam excitation.

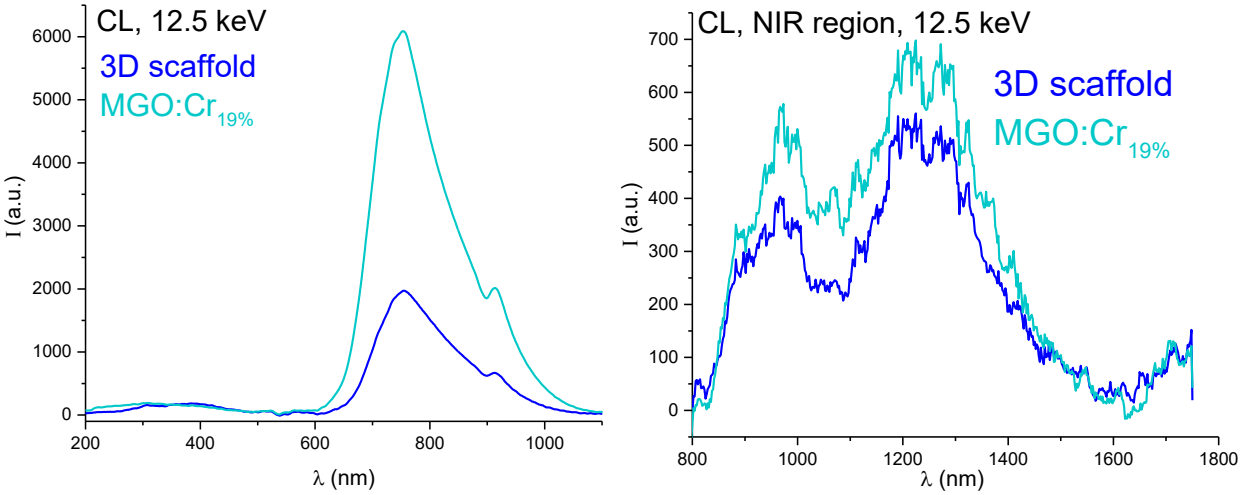

Figure 34. CL emission spectra of 3D scaffold doped with MGO:$Cr_{19\%}$ in both the visible range (left) and the NIR region (right) under electron beam excitation.

3.2.4 Glass-phosphor composite doped with MGO:$Cr_{19\%}$

The MGO:Cr19% sample was doped into the phosphate glass matrix by the DDM method. The PL and CL properties of the fabricated glass-phosphor composite (DDM glass) were measured and described in this chapter.

All recorded PL spectra of DDM glass, reference glass, and phosphor are shown in **Figure 35**. When comparing the spectra of these three samples, it is noticeable that DDM glass exhibits emission identical to that of phosphor under both UV and NIR excitation. However, the emission intensity in the NIR-II region is noticeably weaker.

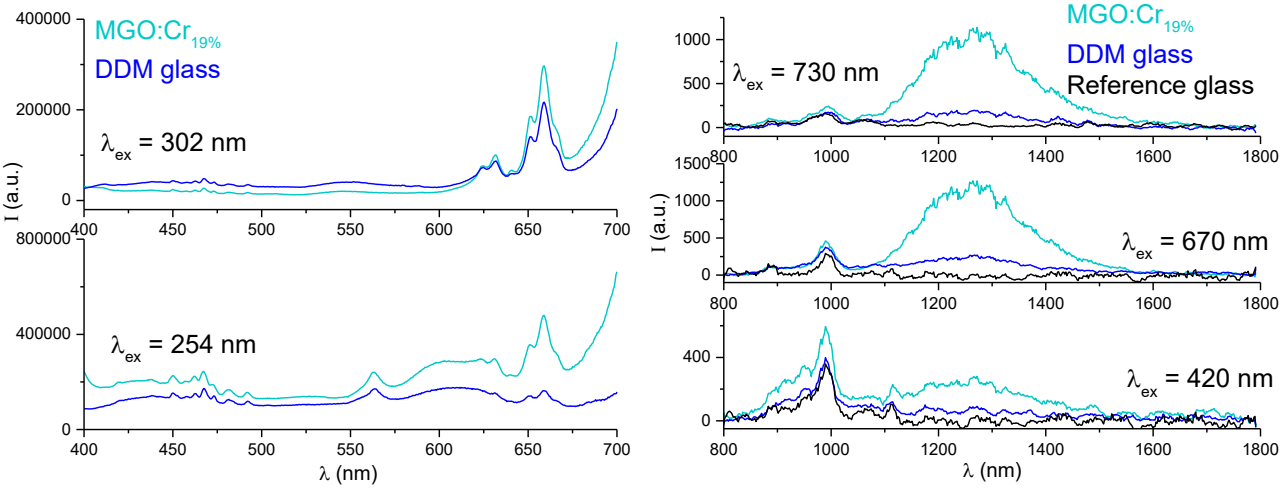

Figure 35. PL emission spectra of the DDM glass sample doped with MGO:$Cr_{19\%}$.

Figure 36 shows photographs of the DDM glass sample under room lighting (**a**), under electron beam excitation (**b**), and after its turning off (**c**). In the first photograph, it can be seen that part of the phosphor was not doped into the glass matrix but remained on the glass surface. Therefore, under

electron beam excitation, a bright red emission identical to the emission of the phosphor itself can be seen. It is also interesting that even though the phosphor does not demonstrate PeL properties, an orange PeL emission was noticeable after electron beam excitation in places where it was doped into the glass.

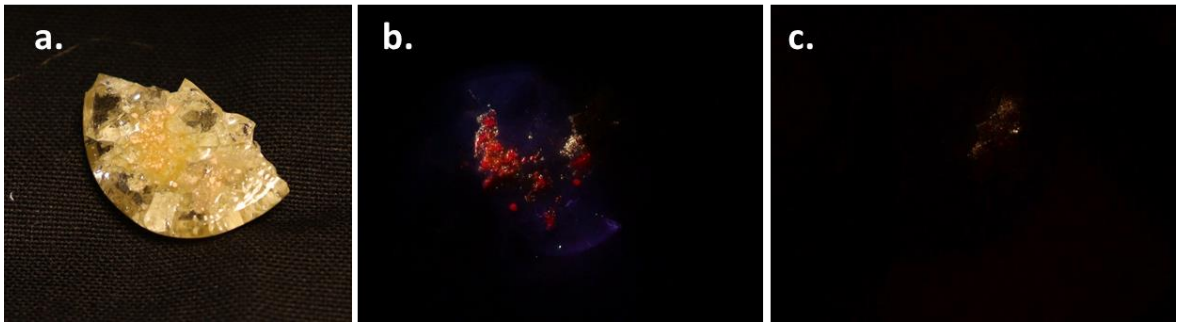

Figure 36. DDM glass sample doped with MGO:$Cr_{19\%}$: **a.** under room lighting; **b.** under electron beam excitation; **c.** PeL after electron beam excitation.

In addition, **Figure 37** shows the recorded CL emission spectra, which demonstrate that the emission of glass and phosphor is identical in both NIR-I and NIR-II regions. It is also interesting that the emission intensity in the NIR-II region of DDM glass is stronger than that of the phosphor itself.

Thus, it can also be said that after doping MGO:$Cr_{19\%}$ phosphor into the glass matrix, the luminescence properties were not only preserved but also modified. It was found that the doped DDM glass shows orange PeL emission after electron beam excitation, and that the CL emission of the doped glass is more intense than that of the phosphor itself. However, it is also worth noting that the DDM method for fabricating glass-phosphor composites is not effective, since the distribution of phosphor powder in the glass matrix is not uniform, and it simply accumulates in one place either inside the glass sample or on the surface, which also leads to the destruction of its structure.

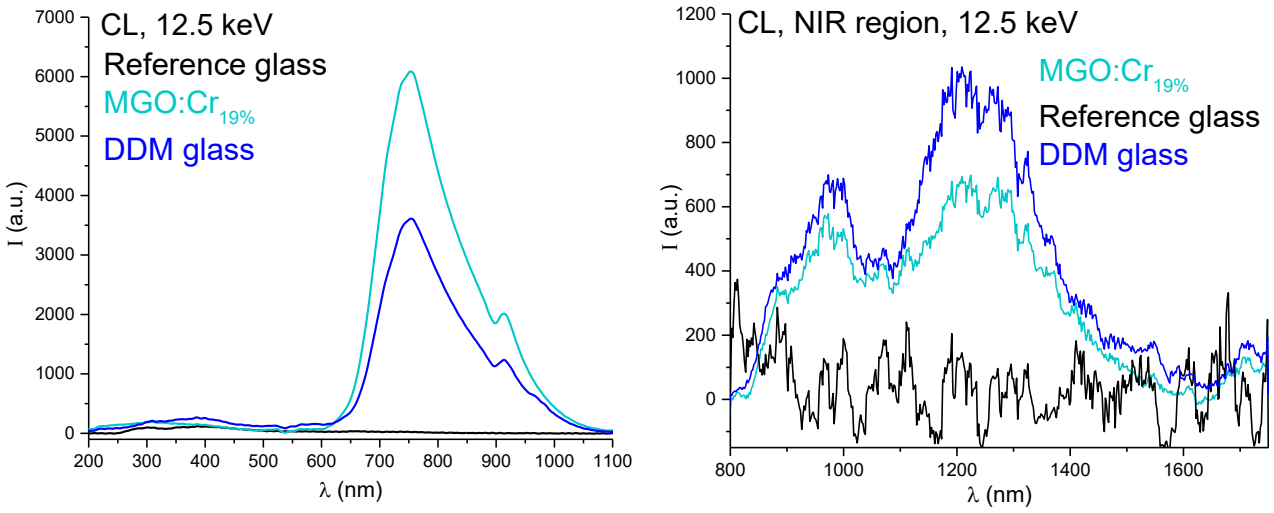

Figure 37. CL emission spectra of DDM glass sample doped with MGO:$Cr_{19\%}$ in both the visible range (left) and the NIR region (right) under electron beam excitation.

4. Conclusion

Based on all the obtained results, it can be concluded that all the aims of this research project were successfully achieved. During the first part of the work, MgO samples doped with Ce^{3+}, Sm^{3+}, and Li^{+} ions were successfully synthesized. The luminescence properties of the doped samples were improved by varying the dopants concentration in the host material. The most significant effect was exerted by increasing the concentration of Li^{+} ions, since they facilitated the doping of lanthanide ions into the host matrix, acting as charge compensators. All doped samples had TL, OSL, PL, CL, and PeL properties. The most promising results were demonstrated by CL and PeL emission spectra.

MgO:$Li_{12\%}Ce_{0.12\%}Sm_{0.24\%}$ sample with the best luminescence properties was successfully doped into the NaPSrO glass matrix and the 3D scaffolds. However, it is worth noting that in the future, it is necessary to take into account that the size of the phosphor crystals should be as small as possible to achieve successful printing of 3D scaffolds using a 3D printer. Glass-phosphor composites were fabricated using three different methods, each with its advantages. However, based on the results, it can be stated that the remelt method is the most promising for this project. The glass sample fabricated by this method demonstrated uniform emission and improved luminescence properties. In general, all fabricated glass-phosphor composites and doped 3D scaffolds exhibited similar optical properties to those of the original phosphor, except for OSL. It was noted that the fabricated samples also showed good CL and PeL properties in the red and NIR regions, which may indicate the potential of the obtained biophotonic glasses in the NIR X-ray excited luminescence imaging.

During the second part of the work, seven batches of MGO samples doped with different ions at different concentrations were synthesized. Doping with such ions as Tm^{3+}, $Ho^{3+,}$ and Nd^{3+} did not

show any effect on the luminescent properties of this phosphor. Whereas doping with $Cr^{3+/4+}$, Mn^{4+}, and Yb^{3+} ions significantly improved and modified the optical properties of the host material. MGO phosphor, in contrast to the first material, demonstrated good PL and CL properties in both NIR-I and NIR-II regions.

Of great importance for this project was the fact that, excited by the NIR light, MGO samples doped with Cr^{3+} ions exhibited PL emission in the NIR-II region. It was also promising that co-doping with Cr^{3+} and Mn^{4+} ions helped enhance CL emission in the NIR-I region. Doping the host material with Yb^{3+} ions added another intense emission band in the range from 900 to 1100 nm (**Figure S2**), which also significantly improved both the PL and CL properties of the phosphor.

From the first two batches, the two best samples were selected and doped into the 3D scaffolds and the NaPSrO glass matrix. Based on all the measured results, it can be concluded that the fabricated glass-phosphor composite and doped 3D scaffolds have the same luminescence properties in the NIR region as the original phosphors, which also makes them potential candidates for the role of biophotonic implants.

However, for more accurate conclusions, a series of additional studies and experiments is required. First, it is necessary to measure the luminescence properties of glass-phosphor composites and doped 3D scaffolds through biological tissue (chicken breast) to determine the depth of light penetration and the emission intensity of the biophotonic implants. Second, to study the effect of doped phosphors on the host body. Finally, to investigate the bioactivity and biodegradation of the glass composites in biological fluids. All of the experiments mentioned above have already been conducted for the glass-phosphor composites doped with MgO phosphor and will be described in detail in the scientific publication. The results will be available after the article is published.

References

1. Oshida, Y. & Miyazaki, T. *Biomaterials and Engineering for Implantology - In Medicine and Dentistry*. (Walter de Gruyter GmbH, 2022). doi:10.1515/9783110740134.

2. Ionescu, M. *et al.* A Brief History of Dental Implants. *Analele Univ. din Craiova - Ser. Istor.* **27**, 149–160 (2022).

3. Chen, Q. & Thouas, G. A. Metallic implant biomaterials. *Mater. Sci. Eng. R Reports* **87**, 1–57 (2015).

4. Hench, L. L. & Polak, J. M. Third-Generation Biomedical Materials. *Sci. American Assoc. Adv. Sci.* **295 (5557)**, 1014–1017 (2022).

5. Farag, M. M. Recent trends on biomaterials for tissue regeneration applications: review. *J. Mater. Sci.* **58**, 527–558 (2023).

6. Yang, Y. *et al.* Mg bone implant: Features, developments and perspectives. *Mater. Des.* **185**, 108259 (2020).

7. Won, J. E. *et al.* Fibronectin immobilization on to robotic-dispensed nanobioactive glass/polycaprolactone scaffolds for bone tissue engineering. *Biotechnol. Lett.* **37**, 935–942 (2015).

8. Hench, L. L. Bioceramics. *J. Am. Ceram. Soc.* **81**, 1705–1728 (1998).

9. Fagerlund, S. & Hupa, L. Chapter 1: Melt-derived Bioactive Silicate Glasses. *Bioactive glasses: Fundamentals, Technology and Applications.* 1–26 (The Royal Society of Chemistry, 2016). doi: 10.1039/9781782622017

10. Rahaman, M. N. *et al.* Bioactive glass in tissue engineering. *Acta Biomater.* **7**, 2355–2373 (2011).

11. Brauer, D. S. & Möncke, D. Chapter 3: Introduction to the Structure of Silicate, Phosphate and Borate Glasses. *Bioactive glasses: Fundamentals, Technology and Applications.* 61–88 (The Royal Society of Chemistry, 2016). doi: 10.1039/9781782622017

12. Pantulap, U., Arango-Ospina, M. & Boccaccini, A. R. Bioactive glasses incorporating less-common ions to improve biological and physical properties. *J. Mater. Sci. Mater. Med.* **33**, (2022).

13. Hench, L. L. The story of Bioglass®. *J. Mater. Sci. Mater. Med.* **17**, 967–978 (2006).

14. Covarrubias, C. *et al.* Osseointegration properties of titanium dental implants modified with a nanostructured coating based on ordered porous silica and bioactive glass nanoparticles. *Appl. Surf. Sci.* **363**, 286–295 (2016).

15. Jones, J. R. Review of bioactive glass: From Hench to hybrids. *Acta Biomater.* **9**, 4457–4486 (2013).

16. Krishnamacharyulu, N., Jagan Mohini, G., Sahaya Baskaran, G., Ravi Kumar, V. & Veeraiah, N. Investigation on silver doped B_2O_3 – SiO_2 – P_2O_5 – Na_2O – CaO bioglass system for biomedical applications. *J. Alloys Compd.* **734**, 318–328 (2018).

17. Abo-Naf, S. M., Khalil, E. S. M., El-Sayed, E. S. M., Zayed, H. A. & Youness, R. A. In vitro bioactivity evaluation, mechanical properties and microstructural characterization of Na_2O-CaO-B_2O_3-P_2O_5 glasses. *Spectrochim. Acta - Part A Mol. Biomol. Spectrosc.* **144**, 88–98 (2015).

18. Wang, H. *et al.* Evaluation of three-dimensional silver-doped borate bioactive glass scaffolds for bone repair: Biodegradability, biocompatibility, and antibacterial activity. *J. Mater. Res.* **30**, 2722–2735 (2015).

19. Abou Neel, E. A., Pickup, D. M., Valappil, S. P., Newport, R. J. & Knowles, J. C. Bioactive functional materials: A perspective on phosphate-based glasses. *J. Mater. Chem.* **19**, 690–701 (2009).

20. Lakhkar, N. J. *et al.* Titanium phosphate glass microspheres for bone tissue engineering. *Acta Biomater.* **8**, 4181–4190 (2012).

21. Richter, R. F. *et al.* Treatment of critical bone defects using calcium phosphate cement and mesoporous bioactive glass providing spatiotemporal drug delivery. *Bioact. Mater.* **28**, 402–419 (2023).

22. Clavijo-Mejía, G. A. *et al.* Bioactivity of radiopaque 45S5 bioactive glass with progressive additions of Bi_2O_3: A dissolution study under static conditions. *Ceram. Int.* **50**, 27216–27226 (2024).

23. Holmström, A. *et al.* Evaluation of bone growth around bioactive glass S53P4 by scanning acoustic microscopy co-registered with optical interferometry and elemental analysis. *Sci. Rep.* **13**, 1–11 (2023).

24. Fu, Q. *et al.* Three-dimensional visualization of bioactive glass-bone integration in a rabbit

tibia model using synchrotron X-ray microcomputed tomography. *Tissue Eng. - Part A* **17**, 3077–3084 (2011).

25. Pei, P. *et al.* NIR-II Ratiometric Lanthanide-Dye Hybrid Nanoprobes Doped Bioscaffolds for In Situ Bone Repair Monitoring. *Nano Lett.* **22**, 783–791 (2022).

26. Wang, F., Zhai, D., Wu, C. & Chang, J. Multifunctional mesoporous bioactive glass/upconversion nanoparticle nanocomposites with strong red emission to monitor drug delivery and stimulate osteogenic differentiation of stem cells. *Nano Res.* **9**, 1193–1208 (2016).

27. Xu, Y. *et al.* Near-Infrared Persistent Luminescence of $CaTiO_3$:Cr,Y for Imaging of Bone Implants Using Red-Light Illumination Instead of X-ray. *ACS Appl. Mater. Interfaces* (2024) doi:10.1021/acsami.4c13865.

28. Yang, Y., Jiang, Q. & Zhang, F. Nanocrystals for Deep-Tissue In Vivo Luminescence Imaging in the Near-Infrared Region. *Chem. Rev.* **124**, 554–628 (2024).

29. Hong, G., Antaris, A. L. & Dai, H. Near-infrared fluorophores for biomedical imaging. *Nat. Biomed. Eng.* **1**, (2017).

30. Jacques, S. L. Erratum: Optical properties of biological tissues: A review (Physics in Medicine and Biology (2013) 58). *Phys. Med. Biol.* **58**, 5007–5008 (2013).

31. Wang, R., Li, X., Zhou, L. & Zhang, F. Epitaxial Seeded Growth of Rare-Earth Nanocrystals with Efficient 800 nm Near-Infrared to 1525 nm Short-Wavelength Infrared Downconversion Photoluminescence for in Vivo Bioimaging. *Angew. Chemie - Int. Ed.* **53**, 12086–12090 (2014).

32. Hong, G. *et al.* Through-skull fluorescence imaging of the brain in a new near-infrared window. *Nat. Photonics* **8**, 723–730 (2014).

33. Lin, C. C. *et al.* A Non-Invasive Method for Monitoring Osteogenesis and Osseointegration Using Near-Infrared Fluorescent Imaging: A Model of Maxilla Implantation in Rats. *Int. J. Mol. Sci.* **24**, (2023).

34. Wang, X. *et al.* Multifunctional Near-Infrared (NIR) Phosphors with NIR I and NIR II Luminescence for Biological Detection. *ACS Appl. Electron. Mater.* **4**, 432–442 (2022).

35. Tummers, Q. R. J. G. *et al.* First experience on laparoscopic near-infrared fluorescence imaging of hepatic uveal melanoma metastases using indocyanine green. *Surg. Innov.* **22**, 20–25 (2015).

36. Yu, D. *et al.* An improved monomeric infrared fluorescent protein for neuronal and tumour brain imaging. *Nat. Commun.* **5**, 1–7 (2014).

37. Tsukasaki, Y. *et al.* Synthesis and optical properties of emission-tunable PbS/CdS core-shell quantum dots for in vivo fluorescence imaging in the second near-infrared window. *RSC Adv.* **4**, 41164–41171 (2014).

38. Hong, G., Diao, S., Antaris, A. L. & Dai, H. Carbon Nanomaterials for Biological Imaging and Nanomedicinal Therapy. *Chem. Rev.* **115**, 10816–10906 (2015).

39. Zheng, B. *et al.* Near-Infrared Light-Excited Upconverting Persistent Nanophosphors in Vivo for Imaging-Guided Cell Therapy. *ACS Appl. Mater. Interfaces* **10**, 19514–19522 (2018).

40. Shang, X. Research on the Advantages and Challenges of Replacing LEDs with Lasers in Functional Near-Infrared Spectroscopy Systems Based on Advanced Signal Processing Algorithms. *Appl. Comput. Eng.* **100**, 14–21 (2024).

41. Smith, A. M., Mancini, M. C. & Nie, S. Bioimaging: Second window for in vivo imaging. *Nat. Nanotechnol.* **4**, 710–711 (2009).

42. Yao, Z., Zhang, B. S., Steinhardt, R. C., Mills, J. H. & Prescher, J. A. Multicomponent Bioluminescence Imaging with a π-Extended Luciferin. *J. Am. Chem. Soc.* **142**, 14080–14089 (2020).

43. Yang, Y. *et al.* NIR-II Chemiluminescence Molecular Sensor for In Vivo High-Contrast Inflammation Imaging. *Angew. Chemie - Int. Ed.* **59**, 18380–18385 (2020).

44. Kosaka, N., Ogawa, M., Choyke, P. L. & Kobayashi, H. Clinical implications of near-infrared fluorescence imaging in cancer. *Futur. Oncol.* **5**, 1501–1511 (2009).

45. Qiu, X. *et al.* Hybrid Nanoclusters for Near-Infrared to Near-Infrared Upconverted Persistent Luminescence Bioimaging. *ACS Appl. Mater. Interfaces* **9**, 32583–32590 (2017).

46. Ding, D. *et al.* X-ray-Activated Simultaneous Near-Infrared and Short-Wave Infrared Persistent Luminescence Imaging for Long-Term Tracking of Drug Delivery. *ACS Appl. Mater. Interfaces* **13**, 16166–16172 (2021).

47. Wang, P. *et al.* NIR-II nanoprobes in-vivo assembly to improve image-guided surgery for metastatic ovarian cancer. *Nat. Commun.* **9**, 1–10 (2018).

48. Liu, H. *et al.* Ultra-Sensitive Detection and Inhibition of the Metastasis of Breast Cancer Cells

to Adjacent Lymph Nodes and Distant Organs by Using Long-Persistent Luminescence Nanoparticles. *Anal. Chem.* **91**, 15064–15072 (2019).

49. Xue, Z. *et al.* X-ray-activated near-infrared persistent luminescent probe for deep-tissue and renewable in vivo bioimaging. *ACS Appl. Mater. Interfaces* **9**, 22132–22142 (2017).

50. Massera, J. *et al.* New alternative route for the preparation of phosphate glasses with persistent luminescence properties. *J. Eur. Ceram. Soc.* **35**, 1255–1261 (2015).

51. Massera, J. *et al.* Processing and characterization of phosphate glasses containing $CaAl_2O_4:Eu^{2+},Nd^{3+}$ and $SrAl_2O_4:Eu^{2+},Dy^{3+}$ microparticles. *J. Eur. Ceram. Soc.* **35**, 3863–3871 (2015).

52. Saarinen, M. *et al.* Persistent luminescent particles containing bioactive glasses: Prospect toward tracking in-vivo implant mineralization using biophotonic ceramics. *J. Eur. Ceram. Soc.* **38**, 287–295 (2018).

53. Zhang, Y., Zhang, W., Zhang, X. & Zhou, Y. Erbium-ytterbium containing upconversion mesoporous bioactive glass microspheres for tissue engineering: luminescence monitoring of biomineralization and drug release. *Acta Biomater.* **168**, 628–636 (2023).

54. Nakanishi, T. *et al.* Enhanced light storage of $SrAl_2O_4$ glass-ceramics controlled by selective europium reduction. *J. Am. Ceram. Soc.* **98**, 423–429 (2014).

55. De Guzman, G. N. A. *et al.* Near-infrared phosphors and their full potential: A review on practical applications and future perspectives. *J. Lumin.* **219**, 116944 (2020).

56. Chang, H. *et al.* Dopant and compositional modulation triggered long-wavelength ultra-broadband and tunable NIR emission in MgO: Cr^{3+} phosphor for NIR spectroscopy applications. *Ceram. Int.* **49**, 309–322 (2023).

57. Zhou, Z., Li, Y. & Peng, M. Near-infrared persistent phosphors: Synthesis, design, and applications. *Chem. Eng. J.* **399**, 125688 (2020).

58. Zhao, F., Song, Z. & Liu, Q. Advances in Chromium-Activated Phosphors for Near-Infrared Light Sources. *Laser Photonics Rev.* **16**, 1–42 (2022).

59. Guckan, V. *et al.* Luminescence of Ce^{3+} and Li^{+} co-doped MgO synthesized using solid-state reaction method. *Nucl. Instruments Methods Phys. Res. Sect. B Beam Interact. with Mater. Atoms* **503**, 53–61 (2021).

60. Oliveira, L. C., Yukihara, E. G. & Baffa, O. MgO:Li,Ce,Sm as a high-sensitivity material for Optically Stimulated Luminescence dosimetry. *Sci. Rep.* **6**, 1–13 (2016).

61. Bishnoi, P. *et al.* Defect modulation and color tuning of MgO: Probing the influence of Sm and Li dopants through x-ray absorption, photoluminescence, and thermoluminescence spectroscopy. *J. Alloys Compd.* **1002**, 175270 (2024).

62. Lee, K. H. & Crawford, J. H. X-ray stimulated luminescence in MgO. *J. Lumin.* **20**, 9–15 (1979).

63. Las, W. & Stoebe, T. TL mechanism and luminescence characteristics in MgO. *Radiat. Prot. Dosimetry* **8**, 45–67 (1984).

64. Devaraja, P. B. *et al.* MgO:Eu^{3+} red nanophosphor: Low temperature synthesis and photoluminescence properties. *Spectrochim. Acta - Part A Mol. Biomol. Spectrosc.* **121**, 46–52 (2014).

65. Kiran, N., Baker, A. P. & Wang, G. G. Synthesis and luminescence properties of MgO: Sm^{3+} phosphor for white light-emitting diodes. *J. Mol. Struct.* **1129**, 211–215 (2017).

66. Oliveira, L. C., Yukihara, E. G. & Baffa, O. Lanthanide-doped MgO: A case study on how to design new phosphors for dosimetry with tailored luminescent properties. *J. Lumin.* **209**, 21–30 (2019).

67. Wang, X. *et al.* A dual-excited and dual near-infrared emission phosphor $Mg_{14}Ge_5O_{24}$:Cr^{3+},$Cr^{4+}$with a super broad band for biological detection. *Dalt. Trans.* **50**, 311–322 (2021).

68. Liang, S. *et al.* Cation Substitution Induced Adjustment on Lattice Structure and Photoluminescence Properties of $Mg_{14}Ge_5O_{24}$:Mn^{4+}: Optimized Emission for w-LED and Thermometry Applications. *Adv. Opt. Mater.* **7**, 1–15 (2019).

69. Patil, K. C., Hegde, M. S., Rattan, T. & Aruna, S. T. Solution Combustion Synthesis of Oxide Materials. *Chem. Nanocrystalline Oxide Mater.* 42–60 (2008) doi:10.1142/9789812793157_0003.

70. Matsukevich, I. *et al.* Mesoporous nanocomposites based on CeO_2 and MgO: preparation, structure and photocatalytic activity. *J. Chem. Technol. Biotechnol.* **98**, 2497–2505 (2023).

71. Ristić, Z. *et al.* Triple-temperature readout in luminescence thermometry with Cr^{3+}-doped

Mg_2SiO_4 operating from cryogenic to physiologically relevant temperatures. *Meas. Sci. Technol.* **32**, 9 (2021).

72. Orante-Barrón, V. R. *et al.* Luminescence properties of MgO produced by solution combustion synthesis and doped with lanthanides and Li. *J. Lumin.* **131**, 1058–1065 (2011).

73. Bolton, J. New NIR emission from Sm^{3+} in Yb^{3+}-Sm^{3+} co-doped tellurite glass. *J. Lumin.* **231**, 117717 (2021).

74. Prasad, V. R., Damodaraiah, S., Babu, S. & Ratnakaram, Y. C. Structural, optical and luminescence properties of Sm^{3+} and Eu^{3+} doped calcium borophosphate phosphors for reddish-orange and red emitting light applications. *J. Lumin.* **187**, 360–367 (2017).

75. Chauhan, V., Dixit, P. & Pandey, P. C. Bi^{3+} assisted luminescence in $SrMoO_4$:Sm^{3+} red phosphors. *J. Rare Earths* **39**, 1336–1343 (2021).

76. Dhoble, S. J., Koao, L., Pawade, V. & Yerpude, A. N. Chapter 2 - Lanthanide-doped $CaAl_4O_7$, $Ca_3Al_2O_6$, $Ca_2Al_2O_5$ phosphors. *Lanthanide-Doped Aluminate Phosphors: Synthesis, Properies, and Applications.* 21–56 (Woodhead Publishing, 2023). doi:10.1016/b978-0-323-90591-6.00001-9.

77. Xu, J. *et al.* $Na_2CaSn_2Ge_3O_{12}$: A Novel Host Lattice for Sm^{3+}-Doped Long- Persistent Phosphorescence Materials Emitting Reddish Orange Light. *Inorg. Chem.* **52**, 13875–13881 (2013).

78. Guérineau, T. *et al.* Laser Direct Writing of Silver Clusters-Based Subwavelength Periodic Structures Embedded in Mid-Infrared Gallo-Germanate Glass. *Adv. Photonics Res.* **3**, (2022).

79. Pokorný, M. *et al.* Gd-admixed (Lu,Gd)AlO_3 single crystals: breakthrough in heavy perovskite scintillators. *NPG Asia Mater.* **13**, (2021).

80. Xue, F. *et al.* A novel rare-earth free red long-persistent phosphor: Mg_2GeO_4:Mn^{4+}. *Ceram. Int.* **43**, 15141–15145 (2017).

81. Zeng, T. *et al.* Crystal Field-Engineered Cr^{3+}-Doped $Gd_3(Mg_xGa_{5-2x}Ge_x)O_{12}$ Phosphors for Near-Infrared LEDs and X-ray Imaging Applications. *Inorg. Chem.* **63**, 12886–12893 (2024).

82. Zheng, D. *et al.* Deep-red to NIR emission of Mn^{4+} and Cr^{3+} doped La_2MgTiO_6 phosphor with multifunctional applications. *J. Lumin.* **257**, 119778 (2023).

83. Capture Landscapes. ISO in Digital Photography [A Comprehensive Guide]. Christian Hoiberg.

https://www.capturelandscapes.com/introduction-iso-digital-photography (Accessed 24.3.2025).

84. Digital Photography Review. What's that noise? Part one: Shedding some light on the sources of noise. Richard Butler. https://www.dpreview.com/articles/8189925268/what-s-that-noise-shedding-some-light-on-the-sources-of-noise (Accessed 24.3.2025).

85. Image Engineering. Image Quality Factors. Color Accuracy. https://image-engineering.de/library/image-quality/factors/1291-color-accuracy (Accessed 29.4.2025).

Supporting information

Table S1. Methods for the fabrication of glass-phosphor composites and phosphor-doped 3D scaffolds.

Phosphors	Glass-phosphor composites	Methods
MgO: $Li_{12\%}Ce_{0.12\%}Sm_{0.24\%}$	3D-printed scaffolds	Doped 3D scaffolds were printed using a nScrypt 3Dn-tabletop printer by the robocasting method. For that, special inks were prepared consisting of glass powder (30 vol%), phosphor powder (10 wt%), and Pluronic F-127 binder acid (70 vol%). First, the calcium phosphate glass ($45P_2O_5$-$2.5B_2O_3$-$2.5SiO_2$-$10Na_2O$-20CaO-10SrO-10MgO) was crushed into a powder with particle sizes < 38 μm, then phosphor was added to the glass powder. After cooling, the glass-phosphor powder was mixed with a Pluronic F-127 binder acid, and then the resulting mass was transferred to a syringe, which was subsequently inserted into a 3D printer. Then, to obtain good samples, the most suitable flux and speed parameters for each of the inks were selected. However, because the size of the phosphor crystals was larger than the nozzle hole, it often clogged. Therefore, some 3D scaffolds were directly extruded from the syringe or printed in a deformed state. After that, to burn the Pluronic acid, the printed 3D scaffolds were heated to 440 °C for 1 h at a heating rate of 1 °C/min. Finally, they were sintered at 550°C for 1 hour, with a heating rate of 5°C/min.
MGO:$Cr_{10\%}Mn_{0.5\%}$		
MGO:$Cr_{19\%}$		
MgO: $Li_{12\%}Ce_{0.12\%}Sm_{0.24\%}$	Remelt glass	Glass with the following composition $50P_2O_5$-40SrO-$10Na_2O$ (NaPSrO) was used as a glass matrix. The remelt method was used to produce the glass-phosphor composite. First, 10 g of a mixture of glass powder and phosphor (5 wt%) was prepared. Then it was melted in a furnace at 950 °C for 7 minutes. The molten mass was poured onto a steel disk to quench. After that, the glass sample was annealed at 400 °C for 6 hours.

	Sandwich glass	The sandwich glass-phosphor composite was obtained in several stages. First, the phosphor was placed on a steel disk in a special form lined with steel rods. Then, the previously melted NaPSrO glass was poured into this form. After the powder adhered to the glass, it was turned over, and the second part of the molten glass was poured on top of the phosphor layer. As a result, a so-called sandwich was formed from two layers of glass and a layer of phosphor between them. Subsequently, the glass was annealed at 400 °C for 6 hours.
	DDM glass	The direct doping method (DDM) was used to produce these two glass-phosphor composites. Based on the name of the method, phosphor (2.5 wt%) was directly added to the molten NaPSrO glass. Before this, 10 g of glass precursors were melted in a furnace at 1050 °C for 20 minutes. Then, the molten mass with added phosphor was poured onto a steel disk for quenching. Subsequently, the obtained glass samples were annealed at 400 °C for 6 hours.
MGO:$Cr_{19\%}$	DDM glass	

Table S2. XRF results of doped MgO phosphors

Doped MgO phosphors	**Compounds/ Concentration (%)**									
	Mg	**Ce**	**Sm**	**Na**	**Si**	**Cl**	**Ca**	**Br**	**Al**	**Sr**
MgO:$Li_{3\%}Ce_{0.03\%}Sm_{0.03\%}$	94.13	0.30	0.40	3.62	0.45	0.65	0.18	0.16	-	-
MgO:$Li_{3\%}Ce_{0.03\%}Sm_{0.06\%}$	95.03	0.35	0.90	-	2.53	0.59	0.53	-	-	-
MgO:$Li_{3\%}Ce_{0.06\%}Sm_{0.03\%}$	83.30	0.42	0.27	14.27	1.40	0.32	-	-	-	-
MgO:$Li_{3\%}Ce_{0.06\%}Sm_{0.06\%}$	83.37	0.42	0.50	13.99	1.38	0.32	-	-	-	-
MgO:$Li_{6\%}Ce_{0.03\%}Sm_{0.03\%}$	83.66	0.22	0.29	13.58	1.57	0.34	0.31	-	-	-
MgO:$Li_{6\%}Ce_{0.03\%}Sm_{0.06\%}$	82.62	0.20	0.51	14.58	1.43	0.35	0.29	-	-	-
MgO:$Li_{6\%}Ce_{0.06\%}Sm_{0.03\%}$	90.32	0.67	0.36	5.78	2.14	0.42	-	-	-	-
MgO:$Li_{6\%}Ce_{0.06\%}Sm_{0.06\%}$	83.52	0.42	0.54	13.34	1.50	0.32	0.31	-	-	-
MgO:$Li_{9\%}Ce_{0.06\%}Sm_{0.06\%}$	90.60	0.58	0.60	5.46	1.87	0.42	-	-	0.22	0.12
MgO:$Li_{12\%}Ce_{0.12\%}Sm_{0.12\%}$	86.78	1.08	1.05	9.28	0.52	0.72	0.15	0.17	0.12	-
MgO:$Li_{12\%}Ce_{0.12\%}Sm_{0.24\%}$	88.48	0.99	2.24	5.97	1.77	0.40	-	-	-	-
MgO:$Li_{12\%}Ce_{0.24\%}Sm_{0.12\%}$	86.22	1.37	0.82	10.98	0.32	-	0.11	-	-	-
MgO:$Li_{12\%}Ce_{0.24\%}Sm_{0.24\%}$	92.57	2.13	2.10	2.10	0.47	-	0.16	-	-	-
MgO:$Li_{24\%}Ce_{0.12\%}Sm_{0.12\%}$	88.84	0.99	1.06	7.02	1.71	0.36	-	-	-	-
MgO:$Li_{24\%}Ce_{0.24\%}Sm_{0.24\%}$	87.03	1.94	2.18	6.54	1.71	0.39	-	-	-	-

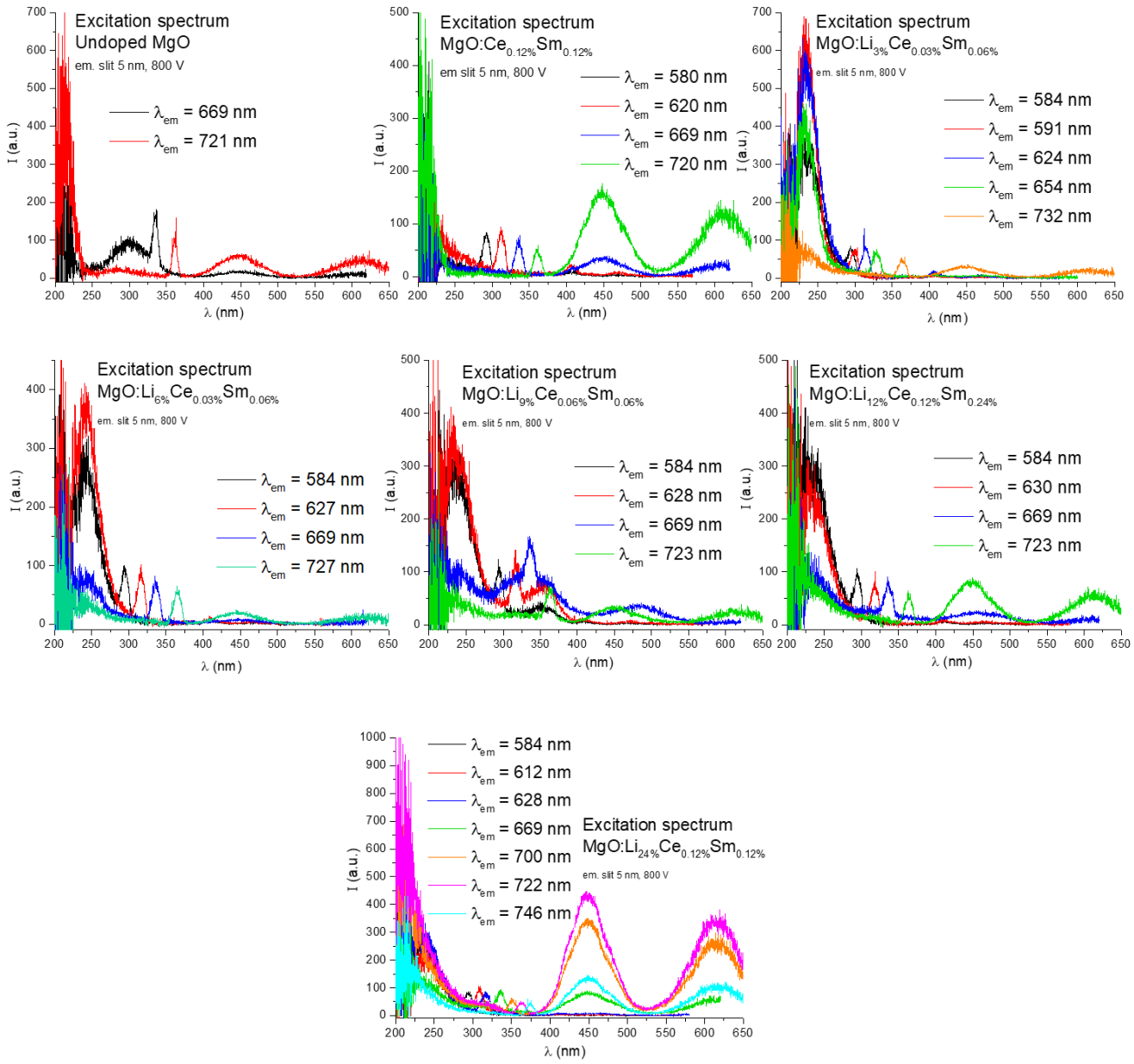

Figure S1. PLE spectra of doped MgO samples.

Table S3. XRF results of doped MGO phosphors.

Doped MGO phosphors	Compounds/ Concentration (%)			
	Mg	Ge	Cr	Mn
MGO	44.53	55.46	260.00 ppm	214.00 ppm
MGO:$Cr_{1\%}$	45.94	53.97	760.00 ppm	70.01 ppm
MGO:$Cr_{3\%}$	46.70	53.10	0.20	191.10 ppm
MGO:$Cr_{5\%}$	47.75	51.94	0.32	214.20 ppm

MGO:$Cr_{7\%}$	48.30	51.01	0.67	248.90 ppm
MGO:$Cr_{10\%}$	50.26	49.13	0.58	234.60 ppm
MGO:$Cr_{13\%}$	33.02	66.02	0.97	345.80 ppm
MGO:$Cr_{19\%}$	49.48	49.14	1.38	202.80 ppm
MGO:$Cr_{10\%}Mn_{0.5\%}$	43.92	55.38	0.64	640.10 ppm
MGO:$Cr_{10\%}Mn_{0.75\%}$	50.49	48.72	0.73	636.50 ppm
MGO:$Cr_{10\%}Mn_{1\%}$	50.46	48.66	0.74	0.13
MGO:$Cr_{10\%}Mn_{1.5\%}$	51.25	51.33	0.92	0.26
MGO:$Cr_{10\%}Mn_{2\%}$	32.64	66.47	0.67	0.20

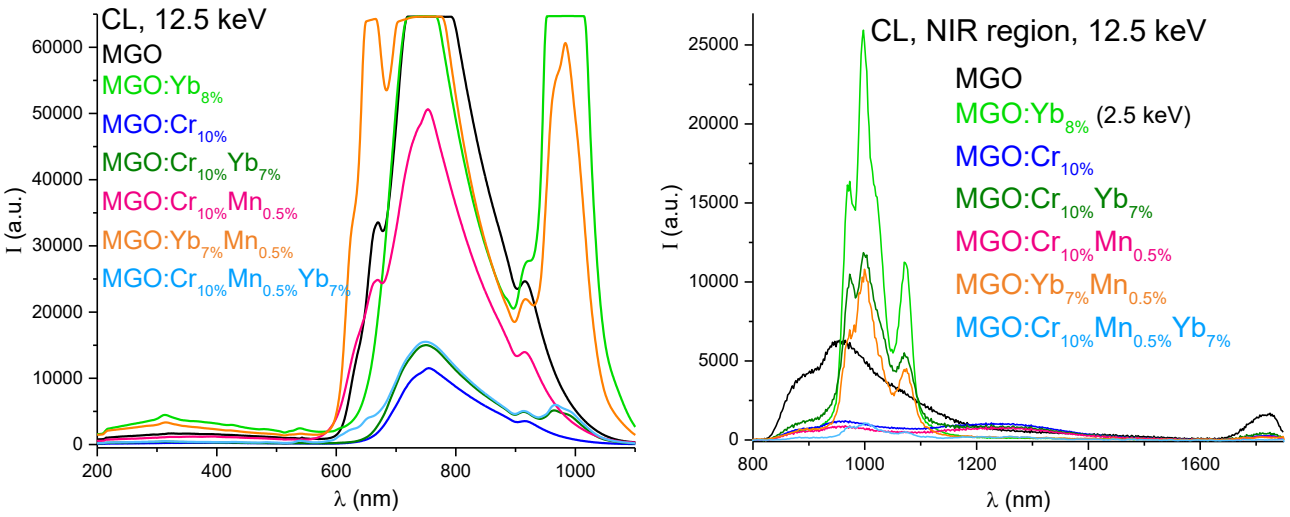

Figure S2. CL emission spectra of doped MGO phosphor from different batches under 12.5 keV electron beam excitation.